The Usumacinta-Grijalva beach-ridge plain in southern Mexico: a high-resolution archive of river discharge and precipitation

Kees Nooren[1], Wim Z. Hoek[1], Tim Winkels[1], Annika Huizinga[1], Hans Van der Plicht[2,3], Remke L. Van Dam[4,5,6], Sytze Van Heteren[7], Manfred J. Van Bergen[1], Maarten A. Prins[8], Tony Reimann[9], Jakob Wallinga[9], Kim M. Cohen[1,7,10], Philip Minderhoud[1] and Hans Middelkoop[1]

[1]Utrecht University, Faculty of Geosciences, 3508 TC Utrecht, The Netherlands;
[2]Groningen University, Center for Isotope Research, 9747 AG Groningen, The Netherlands;
[3]Leiden University, Faculty of Archaeology, 2333 CC Leiden, The Netherlands
[4]Centro Federal de Educação Tecnológica de Minas Gerais, Department of Civil Engineering (CEFET-MG), CEP 30510-000, Belo Horizonte, Brazil
[5]Michigan State University, Department of Earth and Environmental Sciences, East Lansing, MI 48824, United States
[6]Queensland University of Technology, Science and Engineering Faculty, Institute for Future Environments, Brisbane, QLD 4001, Australia
[7]TNO – Geological Survey of the Netherlands, Geomodeling Department, 3508 TA Utrecht, The Netherlands
[8]Vrije Universiteit, Faculty of Earth and Life Sciences, 1081 HV Amsterdam, the Netherlands
[9]Wageningen University, Soil Geography and Landscape Group & Netherlands Centre for Luminescence dating, 6708 PB Wageningen, The Netherlands
[10]Deltares, Department of Applied Geology and Geophysics, 3584 CB Utrecht, The Netherlands.

Correspondence to: Kees Nooren (c.a.m.nooren@uu.nl)

Abstract

The beach-ridge sequence of the Usumacinta-Grijalva delta borders a 300-km-long section of the Southern Mexico Gulf coast. With around 500 beach ridges formed in the last 6500 years, the sequence is unsurpassed in the world in terms of numbers of individual ridges preserved, continuity of the record, and temporal resolution. We mapped and dated the most extensively accreted part of the sequence, linking six phases of accretion to river-mouth reconfigurations and constraining their ages with ^{14}C and OSL dating. The geomorphological and sedimentological reconstruction relied on LiDAR data, coring transects, GPR measurements, grain-size analyses and chemical fingerprinting of volcanic glass and pumice encountered within the beach and dune deposits.

We demonstrate that the beach-ridge complex was formed under ample long-term fluvial sediment supply and shorter-term wave- and aeolian modulated sediment reworking. The abundance of fluvially supplied sand is explained by the presence of easily weatherable Los Chocoyos ignimbrites from the ca. 84 ka eruption of Atitlán volcano (Guatemala) in the catchment of the Usumacinta River. Autocyclic processes seem responsible for the formation of ridge/swale couplets. Fluctuations in their periodicity (ranging from 6-19 yrs) are governed by progradation rate, and are therefore not indicative of sea level fluctuations or variability in storm activity. The fine sandy beach ridges are mainly swash built. Ridge elevation, however, is strongly influenced by aeolian accretion during the time the ridge is located next to the beach. Beach-ridge elevation is negatively correlated with progradation rate, which we relate to the variability in sediment supply to the coastal zone, reflecting decadal-scale precipitation changes within the river catchment. In the Southern Mexican delta plain, the coastal beach ridges therefore appear to be excellent recorders of hinterland precipitation.

1 Introduction

Beach-ridge plains with long sequences holding many individual ridges consisting of coral rubble, shell hash, cobbles, gravel and/or sand are widely distributed across the globe. They have developed along marine and lakeshores under favourable wind and wave conditions, and sufficient long-term sediment supply.

During the past few decades, research on beach-ridge sequences has progressed from describing their morphology and possible origins (Taylor and Stone, 1996; Otvos, 2000) to enabling their usage for palaeoenvironmental reconstructions. They can be used to assess external controls of (relative) sea-level rise, land subsidence, variations in storm impact, and changes in climate and upstream land use (Scheffers et al., 2012; Tamura, 2012 and references therein). They also may include markers left by catastrophic events like volcanic eruptions (Nieuwenhuyse and Kroonenberg, 1994; Nooren et al., 2017), and host soils that are suitable for chronosequence studies (Nielsen et al., 2010; May et al., 2015; Hinojosa et al., 2016).

The number of preserved ridges determines the extent of the palaeo-environmental record stored in the associated sediments, with resolutions up to decadal scale (cf. Curray et al., 1969; Nielsen et al., 2006; Milana et al., in press). The largest beach-ridge plains with multiple parallel beach ridges are formed along medium- to low-energy shorelines of lakes and seas. The beach-ridge plain on the seaward margin of the terrestrial Usumacinta-Grijalva delta in southern Mexico (Fig. 1a) is probably the world's largest. Since the significant reduction in the rate of postglacial sea-level rise in the mid-Holocene, hundreds of semi-parallel sandy beach ridges formed across a shore-perpendicular distance of more than 20 km. In our study area near Frontera (Fig. 1b) beach ridges include aeolian topsets composed of backshore-fringing foredunes. In this paper, we use Otvos's (2000) broad definition of beach ridges, including all 'relict, semi-parallel, multiple ridges' formed by waves (berm ridges), wind (multiple ridges originating as foredunes) or a combination of both.

Earlier morphological studies (Psuty, 1965, 1967; West et al., 1969) identified three main phases in the development of the Usumacinta-Grijalva beach-ridge plain, each linked to a specific position of the rivers' main channels (Fig. 1b). The north-easterly branches of the Grijalva fan-delta river system created favourable conditions for local beach-ridge-complex initiation and development during Phase 1, the Usumacinta (with the San Pablo y San Pedro River (SP y SP in Fig. 1b as the main outlet) during Phase 2 and both rivers (though a combined outlet near Frontera) during Phase 3. Psuty (1965, 1967) proposed an important role in storm surges and overwash in the formation of the beach ridges. Aguayo et al. (1999) established a preliminary chronology of beach-ridge formation on the basis of radiocarbon-dated bivalves and gastropods. Our study elaborates on these pioneering works, aiming to establish a robust chronology for the beach-ridge sequence and to understand the apparent periodical variations in beach-ridge height that are seen in LiDAR imagery of the study area (Fig. 2a).

In the long-term (10^3 years), the considerable accretion of the beach ridge complex has been driven by steady sediment supply by the Usumacinta and Grijalva Rivers (West et al., 1969). Much of this sediment has been generated in their upper catchments and routed through the delta plain to the coastal zone. Morphometric variations between the main phases of beach-ridge formation (Fig. 1b) is mainly influenced by spatiotemporal variability in the positions of the river mouths, size of the feeding river and magnitude of sediment fluxes carried by the water. Studies on other beach-ridge systems suggest that shorter term (10^1-10^2 years) variability can reflect oscillations in river-mouth sediment supply (Brooke et al., 2008a; Tamura, 2012), potentially making the Usumacinta-Grijalva beach-ridge sequence a proxy record for variability in precipitation in the hinterland.

To test this hypothesis, we conducted a detailed geomorphological and sedimentological field study, linking LiDAR data to cored and geophysically surveyed transects, and extensive sediment analyses and dating. Our study covers 150 km of the beach-ridge complex in a shore-parallel direction and 20 km in a shore-normal direction. Grain-size and mineralogical analyses are potentially powerful tools to understand transport and deposition mechanisms of beach-ridge sands (cf. Visher, 1969), but have scarcely been applied in recent beach-ridge studies (exceptions are Guedes et al., 2011; Garrison et al., 2012). Volcanic glass and pumice fragments are highly informative components of the beach-ridge sands (Nooren et al., 2017), and have been chemically fingerprinted to determine their provenance. The internal architecture of the beach ridges was imaged with ground-penetrating radar (GPR), as in other beach-ridge and coastal-barrier studies (e.g. Jol et al., 1996; Van Heteren, 1998; Bristow and Pucillo, 2006; Forrest, 2007; Oliver, 2016).

A detailed chronology of the sequence was established from the combined deployment of Optically Stimulated Luminescence (OSL) on quartz grains (quartz content of the sand is 50 to 65%, Aguayo et al., 1999), and AMS ^{14}C dating of thin layers of terrestrial organic debris (leaf fragments) in the beach-ridge sand. Here we expand on the chronology of a 3-km-long beach-ridge subsection documented in Nooren et al. (2017). Quartz-grain OSL dating has been widely used for establishing the age of coastal deposits in general (e.g. Ballarini et al., 2003; Nielsen et al., 2006; Reimann et al., 2011) and beach-ridge sequences in particular (Tamura, 2012 and references therein; Oliver et al., 2015; Rémillard et al., 2015; Vespremeanu-Stroe et al., 2016; Milana et al., in press), but its combination with AMS ^{14}C dating of thin organic debris layers is presented here for the first time. It provides a unique opportunity for cross-validating the methods.

2 Geographical Setting

The study area is part of the beach-ridge system along the edge of the Holocene Usumacinta-Grijalva delta plain, and stretches from Paraiso in the west to Ciudad del Carmen in the east (Fig. 1b). The delta plain and its hinterland have a humid tropical climate with mean annual precipitation ranging from 1000 to 1500 mm in the highlands of the Chiapas Massif and along the Tabasco coast to locally more than 5000 mm in the mountain foothills in between (West et al., 1969; Hijmans et al., 2005). Approximately 80 % of the annual precipitation falls in a rainy season that lasts from June until November. The excess or effective precipitation contributing to river discharge is around 40-60 % (Table 1). Peak discharges are related to the passage of large tropical depressions, most frequently occurring in September and October.

The drainage basin of the Usumacinta River is dominated by a Cretaceous limestone plateau, folded during the Paleogene (Padilla and Sanchez, 2007), with elevations rarely exceeding 700 m above mean sea level (m+MSL). The headwater catchments of this river, however, are composed of pre-Mesozoic plutonic, metamorphic and volcanic rocks (Fig. 1a). These uplands are dotted with large remnants of Los Chocoyos ignimbrites left by a Pleistocene caldera-forming eruption at Atitlán volcanic centre in southern Guatemala. The Los Chocoyos ignimbrites are also found in the upper drainage basin of the Grijalva River, up to 130 km from the Atitlán caldera (Sánchez-Núñez et al., 2015), but to a smaller extent as the deposits within the Usumacinta drainage basin.

Presently, routing of sediment from upstream to downstream reaches of the Usumacinta River is blocked by the Chixoy hydroelectric dam at Pueblo Viejo (Fig. 1a). This man-made obstacle has reduced sediment transport to the coast since its completion in 1983. High erosion rates have caused rapid infill of the reservoir behind the dam. Between 1983 and 2009, approximately $158 \cdot 10^6$ m^3 of sediment has accumulated at an average rate of $6.1 \cdot 10^6$ m^3/year (Jom Morán, 2010). The total volume of upland source material and the rate at which it is transported downriver show that the Usumacinta could have contributed a sufficient amount of sediment for the rapid progradation of the beach-ridge plain. Nieuwenhuyse and Kroonenberg (1994) demonstrated a similar important role of volcaniclastic sediments in the formation of Holocene beach ridges in Costa Rica.

The coastal zone experiences a diurnal tide with a microtidal range between 0.25 and 0.75 m. During most of the year, low-energy waves coming from the northeast with swells of 0.3 to 0.7 m high produce a wave-generated longshore current carrying river sediments westwards (West et al., 1969). Under these fair-weather conditions, beach accretion is common (Psuty, 1965, 1967), building out the promontories of active river mouths. Usually some 20 to 25 'Nortes' or frontal storms hit the area between October and March. These produce strong north-westerly winds generating swells of 1.2 to 1.7 m as well as local longshore-current reversals and commensurate beach erosion (West et al., 1969). Wave climate increases westward in the dominant longshore-current direction, a result of relatively steeper shoreface slopes in the western part of the study area (notice 10-m depth contour in Fig. 1b). Newly formed beach ridges are rapidly colonised and stabilised by vegetation, most noticeably and dominantly by *Ipomoea pes-caprae*, a salt-tolerant coastal pioneer species (Castillo et al., 1991; Gallego-Fernández and Martínez, 2011). Hurricanes are a frequent phenomenon in the Gulf of Mexico (e.g., Kossin et al., 2010), but they generally pass over the middle and northern part, whereas landfall at or near the study site is rare (www.nhc.noaa.gov/data/#tracks_all).

3 Materials and Methods

3.1 Geomorphological and sedimentological survey

The LiDAR data (Fig. 2a) were originally acquired in April-May 2008 and processed by Mexico's National Institute of Statistics and Geography (INEGI). The derived DEM product has a cell size of 5x5 m, has cm-scale vertical resolution and is accurate to 0.15-0.30 m (Ramos et al., 2009). The LiDAR imagery is used to morphometrically distinguish main and sub-phases of progradational beach-ridge formation, focusing on internal similarity in ridge dimensions, orientation, and lateral and cross-cutting relationships with river-channel morphology. We identified and defined sub-phases that correspond to periods of relatively stable river-mouth configurations, with smaller and larger river-network reconfigurations as the breaks between. LiDAR-inferred morphometric phases were ground-truthed using sediment composition and chronometric results from four field campaigns in the period 2011-2015. To describe and sample the sandy, waterlogged lithology, sediment cores reaching 4 to 11 m depth were taken with a soil auger and a Van der Staay suction corer (Van de Meene et al., 1979). Boreholes were placed along three shore-normal (A, B and C) and two shore-parallel (D1 (youngest beach ridge) and D2) transects (Fig. 2a). To support the interpretation of the grain-size data, surficial nearshore sediments were sampled off Playa La Estrella in April 2013 for modern-analogue study of the shore-normal sorting processes.

The shore-parallel transects aimed at characterising the aeolian facies encountered on the most recent beach ridge, and the swash facies encountered at ~1 m below MSL in a relatively elevated fossil beach ridge. The shore-normal transects aimed at establishing the progradational chronology and its relation with river shifts, with densest sampling along Transects A and B (Fig. 2b). A 3-km-long subsection of Transect A, containing evidence for a volcanic eruption of El Chichón in 540 CE, was studied in substantial detail (Nooren et al., 2017). For consistency, each coring location was chosen at the seaward foot of an individual ridge, except when the aeolian cap on top of the ridges was sampled. Bagged samples of sand were collected at 0.2-0.5 m core-intervals. Encountered organic debris-rich layers were sampled and stored in a cold room (4^oC) pending further processing for AMS ^{14}C dating. For OSL dating, nineteen samples were collected in 30-cm-long opaque tubes from the bottom of shallow hand-augered boreholes during the dry seasons of 2012 and 2013. OSL sample 450 was collected from a soil pit dug in a beach ridge for use in a chronosequence study (Hinojosa et al., 2016).

More than one thousand sand samples were collected in the field, transported to the Netherlands, dried at 105 ^oC, and stored at room temperature. Magnetic susceptibility was measured on all dried sand samples with a hand-held ZH Instruments SM 30. Calcium carbonate was measured on sand samples from the two shore-parallel transects and on sand samples from cores 192, 252, 432, 433, 435, 452 and 453 (Fig. 3), to estimate the maximum depths of pedogenic decalcification, which indicates the position of the phreatic surface (ground water level and, by proxy MSL). Calcium carbonate was measured with a Scheibler Calcimeter, by adding 10% HCl solution to 1 g sediment and measuring the produced CO_2 volumetrically. Carbonate content is expressed as weight percentage $CaCO_3$. Grain-size analyses (range 0.15 – 2000 µm) were conducted with a Sympatec HELOS/KR laser diffraction particle sizer, equipped with an advanced wet disperser (QIXEL). Before measurements, organic matter and carbonates were removed with 20% H_2O_2 and 10% HCl. Grain-size parameters (median, sorting, skewness and kurtosis) were calculated conform the logarithmic method of moments (Folk and Ward ,1957; Blott and Pye, 1975).

Grain-size and magnetic-susceptibility investigations were supported by a limited number of heavy-mineral analyses to characterise the source material. Heavy minerals were separated with a heavy-liquid solution (Sodium Polytungstate, $Na_6[H_2W_{12}O_{40}]$) with a density of 2.85g/cm^3, and identified under a polarised-light microscope. Volcanic glass shards and a pumice clast retrieved from four beach-ridge cores along Transect A, covering a large temporal range in beach-ridge formation (Fig. 2b and 3a, samples 336, 252, 193 and 197), were chemically fingerprinted to identify the eruption source(s). Major-element compositions of the glass shards were determined on 5-12 particles per sample with a Jeol JXA 8600 microprobe equipped with five wavelength-dispersive spectrometers. Measurements were performed by WDS using 15kV acceleration voltage, 10nA beam current and a defocused beam (5µm spot size) to minimise mobilisation of sodium. Instrumental performance and calibration were monitored by repeated analyses of natural glass standards (rhyolitic USNM 72854 VG-568 and basaltic USNM 111240 VG-2) and in-house mineral standards.

3.2 AMS radiocarbon and OSL dating

Within the beach ridges, 1- to 5-cm-thick layers of organic debris were commonly found, especially at locations relatively close to a (former) river mouth (Transects A and B3). The layers contained charcoal, wood and leaf fragments, often mixed with shell fragments. This organic material is transported to the coast by the rivers, then further distributed by longshore currents to eventually be incorporated into the beach ridge facies. The debris is a mixture of apparently younger (hardly physically weathered) and older (rounded edges) reworked material. Reworking was especially evident from the commonly rounded edges of wood and charcoal fragments in the detritus cocktail. Reworked organic material was purposely avoided in our sampling (apart from test samples to demonstrate the associated danger of age overestimation) and age-distance modelling.

Thirty-five terrestrial macro-remains (mainly leaf fragments), isolated from organic debris layers, were standard AAA pretreated, and ^{14}C dated using an AMS facility (Van der Plicht et al., 2000). Ages were reported in yr BP, using the Libby half-life and corrected for isotopic fractionation via $\delta^{13}C$ (Mook and Van der Plicht, 1999). They were calibrated with the software package OxCal 4.2 (Bronk Ramsey, 2009) using the IntCal13 calibration curve (Reimer et al., 2013).

Twenty OSL samples were dated using Risø TL/OSL DA15/20 readers (Bøtter-Jensen et al., 2003), equipped with $^{90}Sr/^{90}Y$ beta source. About 130 g material from the (light-exposed) outer parts of the sample tubes was used for dose-rate determination. High-resolution gamma spectrometry was used to determine radionuclide-activity concentrations (^{40}K, and several nuclides from the U and Th decay chains). Measured values were converted to environmental dose rates using conversion factors of Guerin et al. (2011), assuming immediate burial of the samples to present depth, and accounting for attenuation due to water and organic material (Aitken, 1998) and cosmic-ray contributions (Prescott and Hutton, 1994). For OSL samples obtained from below the groundwater table, a water content of 25 ± 5% by weight was used (pore space fully water saturated), assuming permanent saturation over the entire burial period. For some of the older samples, it is likely that they were deposited above contemporary groundwater levels (Fig. 3b). However, at this stage it is not possible to make a more realistic estimation of the average water content over the entire burial period. Dependency of dose rates and hence OSL ages on water content, implies that OSL age estimates will decrease by approximately 1 % for each weight % decrease in water content (Aitken, 1998). For two OSL samples taken above the groundwater table, a water content of 5 ± 3 % was used (moisture contents at field capacity).

OSL samples were prepared following standard procedures including sieving and chemical treatment with H_2O_2, HCl and HF, to yield sand-sized purified quartz of 212–250 µm. For aeolian sample 179, the fraction 180-212 µm was used. Quartz OSL signals were detected through a 7.5 mm Hoya U340 filter, and an early background approach was applied to obtain a net signal that is dominated by the fast OSL component of quartz (Cunningham and Wallinga, 2010). The OSL IR depletion ratio of Duller (2003) was used to check for feldspar contamination. Equivalent doses were determined on small aliquots (2 mm, ~60 grains) using the Single Aliquot Regenerative dose procedure (Murray and Wintle, 2003). The Central Age Model (CAM, Galbraith et al. 1999) was used to determine over-dispersion in the resulting equivalent-dose distributions (i.e. spread in results on individual aliquots that is not explained by the analytical uncertainties) and for burial-dose estimation. In case of high over-dispersion (>30%) in combination with skewed dose distribution (sample 444), the burial dose was estimated using a bootstrapped version of the Minimum Age Model (Cunningham and Wallinga, 2012). OSL ages are determined by dividing the sample burial dose by the sample dose rate and reported in Year CE, with 1-sigma uncertainty ranges. For each sample, validity of the OSL age was assessed on the basis of the equivalent-dose distribution.

The full set of calibrated AMS ^{14}C and OSL ages was used to establish an age-distance model, using the P_sequence module of the Oxcal 4.2 programme (Bronk Ramsey, 2009; 2016). We furthermore demonstrate the variability in age-distance models for part of Transect B if we assume a constant aeolian accretion rate, following the approach of Minderhoud et al. (2016).

3.3 Ground-penetrating radar

The GPR method is based on the transmission and propagation of electromagnetic energy, commonly at frequencies between 25 and 1000 MHz. It has become a popular non-invasive tool to characterize the sedimentary structures of coastal landforms (Neal, 2004; Tamura, 2012; Van Dam, 2012). To generate 2D images of the subsurface, a pair of transmitting and receiving antennas is moved across the surface, while collecting measurements at regular, pre-defined intervals. Signal reflections are caused by contrasts in dielectric properties between layers, which in turn, are induced by changes in textural properties and water content, among others (Van Dam and Schlager, 2000).

GPR surveys were conducted at the end of the dry season in June 2012 along parts of the transects (Fig. 2a). Data were collected using a MALA ProEx system with 250-MHz shielded antennas and an odometer wheel for accurate positioning (0.1 m step size). Processing of the data included signal dewow to remove low-frequency content, a custom gain function to amplify deeper reflections, background removal below the direct waves to reduce the effect of antenna ringing, and topographic correction. For the time-depth conversion, we used signal velocities of 0.125 (based on the move-out of diffraction hyperbolas) and 0.06 m/ns for deposits above and below the groundwater table, respectively. Interpretation of the internal structures was guided by common criteria for GPR facies analysis, including reflection continuity and amplitude, dip angle, and reflection terminations (van Overmeeren, 1998; Dogan et al., 2011).

3.4 Beach-ridge elevation and accretion volumes

Fifteen shore-normal ribbon-shaped elevation transects (Fig. 2b) were sampled from the LiDAR based DEM, and combined with the dating information to calculate the temporal variability in beach-ridge elevation and accretion volumes. To exclude short-term variability in beach-ridge elevation and to minimise the effect of local erroneous elevation values we divided the 1-km-wide ribbons into multiple polygons (Fig. 2b). Each polygon included at least one, but on average a few ridge/swale couplets.

We estimated an average thickness for the Holocene sandy beach-ridge complex of 10±2 m, based on geophysical tests conducted near the current combined Usumacinta-Grijalva River outlet (Administración Portuaria Integral de Dos Bocas S.A. de C.V., 2005). Unfortunately, we have limited information regarding the inland spatial variability in thickness of the beach ridge complex, and our deepest Van der Staay core of 11 m (core 426, Figs. 3a and 4) did not penetrate the base of the Holocene beach-ridge deposits at this location.

Aeolian accretion sub-volumes were calculated from the ribbon-averaged estimated mean beach-ridge elevation. The calculation assumed all sandy deposits above an estimated average swash run-up height of 0.5 ± 0.5 m above MSL at the time of beach-ridge formation to be aeolian in origin. We used our decalcification depth observations (which sits decimetres deeper than the current groundwater level at more inland beach ridges) and the resemblance of this signal with Gischler and Hudson’s (2004) sea-level curve for Belize, to assess the MSL positions at the time of beach-ridge formation. The calculations were performed for Phase 2 and Phase 3. Along Transect A we added 1 m to the raw LiDAR DEM values because the surface elevations as estimated during the fieldwork period were systematically 1 m higher than the first-generation DEM product for this subarea. We assume that the groundwater level by the end of the dry season in 2012 and 2013 should at least correspond to or be above present MSL, as was the case at core locations along Transects B and C. Given the temporal and spatial variability in run-up height, the uncertainties in the absolute elevation of beach ridge sand samples, late Holocene estimated RSL rise, and the limited number of grain size data, calculated aeolian accretion rates must be regarded indicative only.

4 Results

4.1 LiDAR DEM analyses

The three main phases in beach-ridge formation (Psuty, 1965, 1967; West et al., 1969) are easily discernible from the LiDAR-based DEM (Fig. 2a). Approximately 500 beach ridges can be distinguished. Their spacing is typically between 20-100 m, and mean surface elevations along the three shore-normal transects vary between 0.5 and 3.5 m+MSL (Fig. 3). Beach ridges are relative low and widely spaced near (former) river mouths. Away from a river mouth they merge or become more closely spaced. Beach-ridge elevation, however, tends to increase with distance from a river mouth. The most elevated beach ridges (up to 5 m+MSL) are found in the western part of the study area (Fig. 2a) – on the downdrift side of the system. The influence of drift direction is also apparent in the modest asymmetry of the truncated Phase 2 promontory at the mouth of the SP y SP River and in the strong westward deflection of the mouth of the Gonzalez River (Fig. 2b).

Two faults (Fig. 2b), 0 - 45^0 perpendicular to the orientation of the beach ridges, may be responsible for the slight eastward dipping tilt of ridges in this part of the study area. The DEM shows no evidence for any significant horizontal displacement along NW-SE oriented strike-slip faults described by Aguayo et al. (1999).

Scour holes, possible features produced by large storm surges, are clearly identifiable along only one beach ridge in the western part of the study area (Figs. 2b and B1), and washovers are not apparent from the DEM, indicating that few extreme storm events left clear traces in the area.

4.2 Beach-ridge chronology

The 35 AMS ^{14}C and 20 OSL sample ages (Figs. 2b, 3 and 4, Tables A1 and A2) offer a significant refinement of the preliminary beach-ridge chronology proposed by Aguayo et al. (1999) on the basis of radiocarbon-dated shell material. The resolution offered by the large number of dated samples facilitated the development of age-distance models for the progradation of the beach-ridge plain (Figs. 3 and 4), used in turn to reconstruct the palaeoshorelines as indicated in Figure 5a.

The sequence of calibrated ^{14}C ages shows very good internal consistency, with only two statistically significant age reversals (both in Transect A2; Fig. 4c). This more than fair agreement of ^{14}C ages with vertical stratigraphic order and lateral geographic position gives confidence to their representativeness for deposition age. Nevertheless, dated organic detrital fragments give '*Terminus Ante Quem*' ages that may be older than the beach-ridge sand in which they were entrained. Charcoal fragments have been found to be many hundreds of years older than the more fragile leaf fragments from the same debris layer (Fig. 3a and Table A1, sample 252 and 336), and do not provide a reliable age of final deposition. We therefore avoided wood and charcoal in our sample analysis and only used dated leaf fragments for the age-distance models (Fig. 3). Of all the terrestrial macro-remains in the organic debris layers, fragile leaves are assumed to be the least likely to have survived repeated reworking. There are some indications, however, that even the leaf fragments have undergone some reworking, because samples taken farther from the former river mouth in Transect B2, appear to be 200-500 years older than the LiDAR-tracing projected AMS ^{14}C ages of samples taken closer to the river mouth in Transect A (Figs. 3b and B2).

Quartz OSL behaviour of the samples showed suitability for dating. A dose-recovery experiment indicated that a given dose could be retrieved accurately (dose-recovery ratio 0.997 ± 0.014, n=39). Equivalent-dose distributions were normally distributed and showed over-dispersion as expected for well-bleached deposits (average 18%, n=17). For three samples (179, 427 and 444), higher over-dispersion (>30 %) was observed. The reliability of samples 179 and 427 was considered questionable because the equivalent-dose distributions lacked the characteristic skewness that would characterise over-dispersion due to heterogeneous bleaching (e.g. Wallinga, 2002).
Although volcanic quartz from certain types of volcanic deposits has inappropriate OSL properties for dating (e.g. Tsukamoto et al., 2003), Pietsch et al. (2008) demonstrated that OSL sensitivity of quartz increases linearly with fluvial transport distance for the Castlereagh River in Australia. Such a sensitization effect might explain the decent OSL sensitivity of our samples, even if they started as ignimbrites with poor OSL sensitivity in the upper catchment (~1100 km) (see section 4.5). Another explanation could be sought in a secondary source of quartz with high luminescence sensitivity. Even if the bulk of the sediment is from ignimbrites, a minor component from another source may be responsible for the observed OSL signal.

Dose rates were found to vary between 1.83 ± 0.08 and 2.66 ± 0.10 Gy/ka (mean 2.18 Gy/ka). These values are lower than those reported for Usumacinta levee deposits (2.38 – 4.55 Gy/ka, Muñoz-Salinas et al., 2016). The difference is likely related to lower amounts of silt and clay in the beach ridges than in the levees. Dose rates are much higher than the extremely low values reported for the quartz-rich beach ridges in Florida (e.g. Otvos, 2005; López and Rink, 2008; Rink and López, 2010).

Quartz OSL ages are internally highly consistent, and agree well with the calibrated ^{14}C ages (Figs. 3 and 4), underscoring the usefulness of OSL dating in the establishment of beach-ridge chronologies (cf. Tamura, 2012).

For two samples (450 and 451), collected at the same location but at different depths, OSL ages (respectively 2567 ± 260 and 1957 ± 210 BCE) suggested an age difference of about 600 years. A possible partial explanation is that the water-content estimations for these samples (field capacity for OSL sample 451; water-saturated for sample 450) (Table A2) are not correct. If more similar water contents are assumed for both samples, the age difference is much reduced, highlighting the importance of water-content estimation in OSL dating. An alternative, or additional, explanation could be that the sediment above the groundwater table was reworked (e.g. through bioturbation). The spread in equivalent-dose distribution for sample 179 may indicate such reworking, but for sample 451 the equivalent-dose distribution provides no evidence of reworking. For the age-distance model, we excluded OSL ages that were judged to be of questionable validity (179 and 427) and those obtained from sediments above the groundwater table (179 and 451).

The age-distance models for Transects A and B are presented in Fig. 3. For a 3-km section (Transect A2), the age-distance model was published by Nooren et al. (2017; Fig. 4c). Three new OSL analyses (this paper; Table A2 and Fig. 4c), one providing a questionable age (sample 427), corroborate the robustness of that study. Radiocarbon ages of shells reported by Aguayo et al. (1999) do not provide additional age constraints, owing to limitations in accuracy of the shell ages caused by carbon reservoir effects and taphonomic depositional uncertainty.

We ran a P_sequence Bayesian calibration model (k=0.05 m^{-1}) (Bronk Ramsey, 2009), fed with the AMS ^{14}C and OSL dates and relative shore-normal positions, and with boundaries (i.e. discontinuities) prescribed at the transitions between the three main beach-ridge-formation phases. For the age-distance model of Transect B (Fig. 3b), we projected AMS ^{14}C and OSL ages of samples from Transect A, correlating along the beach-ridge traces in the LiDAR data. Because of the assumed time lag between the final burial of leaf fragments in the beach ridges at smaller (Transect A) and greater (Transect B) distance to the river mouth during Phase 2, in the corresponding part of Transect B the ^{14}C ages of samples 185 and 438 (Fig. 3b) were excluded from the model. We identified one OSL age (sample 437) as an outlier (too old compared to ages of neighbouring samples) and excluded it from the age-distance modelling (Fig. 3b).

The age-distance model for Transect A (Fig. 3a) shows a long-term average progradation rate that decreased from 4.1 to 3.4 m/y between the start of Phase 2 (~1800 BCE) until the transition between Phases 3A and 3B, dated at ~1050 CE. Progradation rates returned to higher values during Phases 3B and 3C, 4.0 and 4.5 m/y respectively, related to the reconfiguration of the river system and the avulsion of the Usumacinta River around 1050 CE (discussed in section 5.1).

The age-distance model for Transect B (Fig. 3b) includes a preliminary model for Phase 1 (4500 –1800 BCE). The model is based on relatively few samples, including OSL ages sensitive to uncertainty related to water-content assumptions, and must therefore be treated with caution. The age-distance model for Phase 2 has an age range between 1775 ± 95 BCE and 30 ± 95 CE (at 1σ), which covers a slightly shorter time period than at Transect A where Phase 2 runs until approximately 150 CE. The LiDAR image shows clear signs of truncated beach ridges between Phases 2 and 3 at Transect B, explaining the occurrence of a hiatus. To investigate possible age-distance scenarios for Transect B (Phase 2), we calculated five possible short- and long-range scenarios (Transect B2-1 till B2-5 in Fig. 2b) by including aeolian accretion (see section 4.6) as a proxy for progradation rate of the beach-ridge plain. The depicted scenarios (Appendix B, Fig. B2) assume shore-normal aeolian accretion activity to be constant between 1800 BCE and 30 CE. Under this assumption the most noticeable change in progradation rate occurred around 1000 BCE, during a period when relatively high beach ridges are indicative for a strong drop in progradation rate. This is apparent in both long- and short-range scenarios and at all five transects. The long-range scenarios seem to be in better agreement with the mean of the OSL ages. These calculations show the potential to improve age-distance models with additional information regarding the temporal variability in aeolian accretion rates.

The age-distance model is less reliable for Phase 3A owing to the lack of dated samples along Transect B, the rejection of OSL sample 179 and uncertainties in the projected location of dated samples from Transect A. The age-distance model is very robust again for the period 1050 CE to present (Phases 3B and 3C), with precision of modelled ages in the order of only 10–60 years (at 1σ).

For Transect C the age-distance model (not shown) is preliminary, because it only relies on two AMS ^{14}C dated samples (Table A1), and geomorphological age-projections from Transect A.

4.3 Grain-size analyses

The beach ridges consist of moderately well- to well-sorted fine to medium sand. Because sediment lithology is very uniform at all core locations, and sedimentary microstructures are not recovered in Van der Staay hand corings, core logs are not presented.
All of the over two hunderd analyzed sand samples show a unimodal grain-size distribution with a median between 117 and 350 µm (Fig. 5b). The grain-size of sand samples from two shore-

parallel transects (Fig. 6) show a general coarsening in the dominant (westward) longshore-transport direction.

The longshore trend in grain size is apparent in both swash and aeolian facies (Fig. 6), applies along the full length of the study area, and does not appear to be affected by the deltaic promontory of the Usumacinta/Grijalva River in the middle of it. Skewness of the grain-size distribution increases in the dominant longshore-transport direction, denoting an increase in excess fines, and the swash facies tends to get better sorted (decrease in phi values) in the same westward direction. Kurtosis values do not show systematic changes. Magnetic-susceptibility values also tend to increase in a westward direction, with the most elevated values around the (former) waterline, as heavy minerals, including titanomagnetite, preferentially accumulate in the swash zone (Komar, 2007). The high magnetic-susceptibility values for aeolian beach-ridge sand near the mouth of the currently active Usumacinta/Grijalva and Gonzalez Rivers is likely related to the contribution of volcaniclastic material from El Chichón's 1982 eruption, as magnetite enrichment in the beach-ridge sands also occurred after earlier eruptions of El Chichón (Nooren et al., 2017). The $CaCO_3$ concentration decreases in the longshore transport direction, in line with a decreased influence of calcareous sediment from the calcareous platform in the eastern part of the study area (Ayala-Castanares and Guittiérrez-Estrada, 1990) (Fig. 1b).

The westward increase in median grain size probably relates to an increase in wave energy, which also may have caused the steepening of the shoreface slopes in that same direction. The presence of mega-cusps at beaches near the mouth of the Gonzalez River is an additional indication of relatively strong wave impact on the western side of the system. Similarly, and at first sight contradictory, grain-size coarsening in the longshore-drift direction was observed at St. George Island (Balsillie, 1995) and along the North Sea beaches of East Anglia, England (McCave, 1978). McCave (1978) explained the coarsening of beach sand in the longshore-transport direction as a result of the winnowing of fines and their offshore transport by tidal currents. Similar processes could be responsible for the westward grain-size coarsening, and could explain the dominance of relatively fine clastic sediments on the continental shelf at the study site (Ayala-Castanares and Guittiérrez-Estrada, 1990) (Fig. 1b). The offshore transport of fines is probably stimulated by the anticyclonic eddy that develops during spring and moves westward along the coast during summer (Salas de León et al., 2008). This eddy influences bottom currents, especially west of Usumacinta/Grijalva River outlet. Lastly, it should be noted that deviations from this general pattern in longshore grain-size distribution do occur. The relatively coarser grain size of the three aeolian samples approximately 10 km west of the SP y SP River for example are probably due to the contribution of eroded and reworked sand from the old promontory of the SP y SP River (Fig. 6).

Although the major variability in grain-size parameters occurs in a shore-parallel direction, shore-normal sorting processes due to wind and wave activity have resulted in significant variation in grain-size parameters as well (Fig. 7). Surface samples from the modern beach profile at Playa Estrella (Fig. 7a) show an increase in grain size from offshore towards the coast, with coarsest and least-sorted sand occurring in the relatively high-energy swash zone. The grain-size characteristics of backshore beach deposits and dune/ridge sands are very similar. They differ from the swash deposits in having a reduced presence of coarse grains (more symmetrically skewed) and a better sorting (Figs. 7 and B4). These properties indicate that aeolian processes likely have been in play in the development of backshore deposits and dune ridges.

The grain-size variability in shore-normal direction along Transect A (Appendix B, Fig. B3) is very similar to that of surficial samples taken at the current beach at Playa Estrella. Samples from core 197 (Fig. B3, 0.04 km) reflect shore-normal sorting processes and demonstrate a coarsening-upward sequence with strongly negatively skewed relatively fine sandy deposits at –4 m+MSL, likely deposited in the nearshore zone (Fig. 7a). These deposits are covered by a few meters of fine sand with grain-size parameters resembling the surficial samples from the swash zone (Fig. 7a), consistent with Walther's Law.

Samples from beach ridges formed during Phase 3B (Figs. 4b,B3, and B4) are strikingly different from the general pattern (Figs. 7b and B4), with a higher contribution of well-sorted fine to medium sand, likely related to an increased availability of reworked sand due to the erosion of the SP y SP promontory. The same process is likely responsible for the coarser grain sizes of the aeolian sand samples from the youngest ridge collected 10 km west of the still eroding SP y SP promontory (Fig. 6).

4.4 Internal architecture

Despite the high signal attenuation, which limited the depth of investigation in various areas, the GPR measurements clearly show strong seaward-dipping reflectors in all transects (Fig. 8), with slopes between 2 and 5° (Fig. 4b and 8). Since all GPR transects were oriented perpendicular to the ridges, these angles are close to the actual angles. The values are similar to dipping angles reported by Psuty (1967) for beach deposits elsewhere along this coast. The largest slope angles are preferentially associated with more elevated beach ridges. No reflections hinting at interrupting erosional surfaces are apparent, and strong landward-dipping reflectors were rarely encountered in the GPR-surveyed transects.

The top of the foreshore deposits is located around 0.8 m+MSL (Fig. 8). At depths between 1 and 2 m-MSL, the slopes of the upper-shoreface deposits start to decrease. Reflection terminations (e.g., at x = 82 m and y = 40-50 ns in Fig. 8) suggest the periodic welding of bars onto the beach face. This mechanism of beach progradation by accretion of longshore bars is typically associated with a large sediment supply and longshore sediment transport (e.g., FitzGerald et al., 2000; Aagaard et al., 2004; Tamura, 2012). Unrelated to this bar welding event, the GPR profile shows a few landward-dipping reflections at the top of the beach sequence (at x = 100-110 m and y = 40-50 ns in Fig. 8) that may be associated with the infill of a large runnel that formed when a swash bar merged with the beach.

The GPR results compare well with the extensive investigations conducted at the fine sandy swash-built beach ridges at St. Vincent Island, Florida (Forrest, 2007), confirming the prominence of swash deposits in beach-ridge sequences formed under microtidal conditions and relatively low wave impact. It is hard to distinguish the aeolian radar facies from that of the lithologically similar beach deposits, with the only useful indicator being the termination of seaward-dipping foreshore reflections (red dashed line in Fig. 8). The absence of significant internal erosional surfaces suggests that the ridges formed quickly or at least continuously, uninterrupted by significant coastal-erosion events. Landward-dipping overwash deposits, as described by Psuty (1967; 1969), are not evident in our selected GPR transects (nor did LiDAR data support their presence in the promontory parts of the beach-ridge complexes). The landward-dipping structures in Fig. 8 are situated too deep in the subsurface to be interpreted as overwash deposits.

4.5 Composition and source of beach-ridge sands

The major-element compositions of relatively large sand-sized volcanic glass shards and pumice fragments (250-1500 μm) and a pumice clast of 1.5 cm, isolated from beach-ridge samples along Transect A, are reported in Table A3. The major-element composition is similar to that of the Late Pleistocene Los Chocoyos tephra (Kutterolf et al., 2008), and is significantly different from any of the late-Holocene tephras of El Chichón volcano (Fig. 9) (Nooren et al., 2017). It is therefore inferred that Los Chocoyos ignimbrites have been an important sediment source for the Usumacinta-Grijalva delta. They were emplaced during a mega-eruption at Atitlán volcanic centre around 84,000 years ago (Drexler et al., 1980), which produced an estimated 150 to 160 km^3 Dense-Rock Equivalent (DRE) of tephra fall and some 120 km^3 DRE of pyroclastic flow deposits (Rose et al., 1987). It is the only Late-Pleistocene volcanic eruption that deposited voluminous tephra north of the Motagua River valley (Fig. 1a; Koch and McLean, 1975). The Los Chocoyos pyroclastic flow deposits reach thicknesses of more than 200 m, and have been found well into the watersheds of the Grijalva and Usumacinta Rivers (Instituto Geográfico Nacional, 1970; Koch and McLean, 1975; Rose et al., 1987; Sánchez-Núñez et al., 2015). We estimate that approximately 3 % and 16 % of the pyroclastic flow deposits were deposited in the Grijalva and Usumacinta watersheds, respectively. In the steep and poorly vegetated terrain, these volcaniclastic deposits are vulnerable to erosion and particularly prone to mass transport by landslides (Harp et al., 1981). It is therefore not surprising that abundant volcaniclastic minerals and glass shards (Solis-Castillo et al., 2013) were found in Holocene levee deposits of the Usumacinta River at Tierra Blanca (Fig. 1a), reflecting reworked Los Chocoyos tephra, as geochemical and micromorphological evidence suggests (Table A3, (Cabadas-Báez et al., in press).

The heavy-mineral analyses confirm the presence of volcaniclastic material within the beach-ridge sands. The non-opaque heavy minerals are dominated by green and brown amphiboles, clinopyroxene, titanite and epidote, whereas the opaque heavy minerals are dominated by titanomagnetite.

4.6 Beach-ridge elevation

The temporal variability in beach-ridge elevation along the fifteen cross-normal ribbon-shaped elevation transects representing Phases 2 and 3 is demonstrated in Fig. 10. Most noticeable are the high-amplitude elevation changes along Transect B during Phase 2, and the relatively low standard deviations during periods in which elevated beach ridges were formed. Although swale elevations should preferably not be used as sea-level index points for the reconstruction of relative sea-level (RSL) rise, overall, mean swale elevations along Transects A, B and C show a continuously increasing trend of about 0.3 mm/yr (Fig. 10). This is in line with expected long-term rate of RSL rise in the southern Gulf of Mexico area, and comparable to those of the reconstruction of RSL rise made by Gischler and Hudson (2004) for Belize. The estimated depths of pedogenic decalcification (Figs. 3a and 3b) also supports this RSL curve, but further analyses are needed for better refinement. We found no evidence for a mid-Holocene RSL high-stand followed by a 2-m drop during the late Holocene (e.g. Stapor et al., 1991; Tanner, 1992; Morton et al., 2000; Blum et al., 2003). Rather, our observations are in accord with more recent RSL reconstructions for the northern Gulf of Mexico coast that show a gradual rate of RSL rise during the late Holocene (Törnqvist et al., 2004; Milliken et al., 2008; Donelly and Giosan, 2008).

4.7 Volumetric growth rate of the beach-ridge plain

The total average late-Holocene sediment-accumulation rate was estimated by simply dividing the total volume of beach-ridge deposits along the system's 150 km length by the duration of beach-ridge formation. Assuming an average thickness of 10 ±2 m, the overall average accumulation rate over the period 1800 BCE until today has been 2.3–3.5 million m^3/yr. Accumulation rates along Transects A, B and C range between 16 and 54 m^3/m/yr (Table 2).

The calculated average accumulation rate is exceptionally high compared to those reported for other large beach-ridge systems, such as 0.05 million m^3/yr at Guichen Bay, Australia (Bristow and Pucillo, 2006), 0.14 million m^3/yr at Keppel Bay, Australia (Brooke et al., 2008a) and 1.7 million m^3/yr at Kujukuri, Japan (Tamura et al., 2010). As these systems are much shorter than the Usumacinta-Grijalva plain, accumulation rates are more similar when expressed in m^3/m/yr. For two other large beach-ridge systems with detailed chronological control we estimate accumulation rates of 0.92 million m^3/yr (Nayarit, Mexico; using cross sections in Curray et al., 1969), and 1.4 million m^3/yr (Katwijk, the Netherlands; using sections in Cleveringa, 2000).

Average aeolian accretion rates along Transects A, B and C range between 1.5 ± 1.0 and 6.6 ± 1.9 m^3/m/yr (Table 2), with relatively high values along Transect B during Phase 2 and along Transect A during Phase 3B. Rates are much higher than the average long-term aeolian accretion rates of 0.1 – 0.6 m^3/m/yr for three beach-ridge plains in southeastern Australia (Oliver, 2016) but are relative low compared to average long-term accretion rates for larger-scale foredunes, which roughly vary between 5 and 20 m^3/m/yr (e.g. Aagaard et al., 2004; Ollerhead et al., 2013; Keijsers et al., 2014).

Aeolian accretion rates are ca. 6 - 21% of the total volumetric growth rate of the beach-ridge plain (Table 2), comparable to the 10.5% inferred for the Moruya beach plain, Australia (Oliver, 2016). Aeolian processes therefore play a minor role in beach-plain sediment accretion. We found a relatively large contribution of aeolian accretion (26 ±10% of total beach-ridge accretion) for beach ridges formed along Transect B between approximately 1800 BCE and 30 CE (Phase 2), which could be an indication of stronger north-easterly winds during this time.

4.8 Evolution of the beach-ridge plain

The new chronological, geomorphological and sedimentary data enabled us to reconstruct the three-phased development of the beach ridge complex in considerably more detail than previous researchers.

The oldest part of the beach-ridge sequence (Phase 1) has been most completely preserved on the inland side of the barrier complex, southwest of the current confluence of the Grijalva and Usumacinta Rivers (Tres Brazos, Fig. 2b). Here, beach ridges are partly covered by organic-rich back-barrier marsh deposits that locally reach thicknesses of up to 4 m (e.g. core 307; Fig. 2b). To the east of Tres Brazos (Fig. 2b), no Phase 1 beach-ridge topography is discernible from the DEM. Any Phase 1 ridges were likely eroded over time by the migrating Usumacinta River. Our oldest age of 4248 ±90 BCE (at 1σ) for freshwater organic deposits (sampled in core 307, Fig. 3b), post-dates the onset of coastal progradation in the study area. This organic unit formed after the oldest beach ridges had developed, suggesting that the inception of the Usumacinta-Grijalva beach-ridge plain (i.e. the onset of Phase 1), marking the transition from transgressive to regressive conditions, probably occurred centuries earlier (ca. 4500 BCE).

Relatively coarse-grained beach ridges, inferred to be supplied with sediment by a branch of the Grijalva River, accreted during Phase 1A along the inland part of Transect B (Fig. 5a). This set of beach ridges formed until 2800 BCE, at a time when RSL was several meters lower than today. Nowadays, only the most elevated beach ridges formed during that phase protrude from the marshy plain.

During Phase 1B, which lasted until 1800 BCE, the Usumacinta River system increasingly supplied relatively fine sediment to the area, as its SP y SP distributary developed. The inland part of Transect A shows that the new promontory at the mouth of the SP y SP did not immediately developed the characteristics of a mature beach-ridge plain. At core location PP1 and at Pozpetr (Fig. 3a), only clayey estuarine and organic flood-basin deposits occur. The first beach-ridge sand body only starts near core 336. The few linear structures in the DEM that are discernible further inland may represent chenier-like features (as tentatively indicated in Fig. 3a). The Grijalva River system continued to influence beach-ridge formation in the area of Transect B. During Phase 1B it made use of the 'Popal Grande palaeochannel' (cf. Psuty, 1967), which was active between approximately 2800 and 2100 BCE (Fig. 5).

During Phase 2 (1800 BCE – 150 CE), the SP y SP promontory further developed. Its relative large acute angles between beach ridges and the present-day coastline (Fig. 2), indicate that riverine sediment supply contributed significantly to the growing beach ridge complex. Fluvial contributions from more easterly sources are improbable, because sizeable rivers have not been present east of the SP y SP branch. In addition, calcareous biogenic sediments dominate in that sector of the coastal-lagoonal plain, particularly east of Ciudad del Carmen (Fig. 1b). A marine source area is unlikely as well, because surface sediments in front of the SP y SP river mouth are predominantly composed of clay and fine silt (Ayala-Castañares and Guttiérrez-Estrada, 1990). A possible marine source area for beach-ridge sands is the seabed in the western part of the study area (Fig. 1b), but there is no known mechanism that could have moved vast amounts of sediment against the dominant drift direction. A terrestrial contribution via longshore current, sourced from the Grijalva River mouth, is unlikely for the same reason: the necessary transport path would be opposite the dominant drift direction. Moreover, the main distributaries of the Grijalva River system at the time were positioned farther westward than at present (e.g. the Pajonal and Blasillo palaeodistributaries described by Von Nagy (2003) (Fig. 1b). Towards the end of Phase 2, a slight increase in acute angles of the beach ridges is seen about 5 km west of the present main outlet (Fig. 2a). This local anomaly from the overall pattern indicates temporal activation of a distributary river mouth at this location, which may be seen as a precursor of the nearby main outlet active during Phase 3.

The transition between Phases 2 and 3 is set at regionally truncated beach ridges in the area near Transect B. These features indicate a major reorganisation in the Grijalva and Usumacinta distributary network and river mouths. Around 150 CE, a major new delta promontory began to develop, that still is the joint outlet of the Grijalva and Usumacinta rivers today. In its development, we distinguish three sub-phases. During Phase 3A, the old SP y SP outlet was still functioning. At the end of Phase 3A, the Usumacinta had fully avulsed towards its current location, terminating sediment delivery at the old outlet. The age-distance model of Transect A2 (Fig. 4c) indicates that this latter avulsion occurred around 1050 CE. The break between Phases 3A and B is marked by a shift in beach-ridge orientations. West of the SP y SP abandoned outlet, elevated beach ridges are related to increased sediment supply due to cannibalisation of the former promontory. Even today, the old SP y SP promontory is still eroding, with current rates around 3.5 m/yr (Ortiz-Pérez, 1992; Ortiz-Pérez et al., 2010).
The transition between Phases 3B and 3C, placed at 1460 CE, is not related to river-outlet repositioning and therefore morphometrically more arbitrary. It is reflected by moderate increases in progradation rate (Table 2).

5 Discussion

5.1 Beach-ridge-formation model

Psuty (1965, 1967) suggested an important contribution of storm surges and related overwash to the development of the Usumacinta-Grijalva beach ridges. Our GPR measurements revealed only evidence for swash-built beach ridges with an aeolian cap on top, whereas typical landward-dipping reflections from washovers have not been identified. In addition, the sandy deposits do not include any exceptionally coarse sand layers within the upper part of the cores, and most of the analysed sand samples from above MSL were characterised as aeolian in origin. The DEM of the area shows little evidence of extreme storm events impacting the area; scour holes were only identified along one beach ridge, formed around 1450 CE. Nevertheless, storms do play a role in beach-ridge formation. Strong north-westerly winds during 'Nortes', for example, cause beach erosion (West et al., 1969). Owing to a temporal reversal in the longshore-current direction, sand is transported eastward and contributes to beach-ridge formation several months after the storm event. Individual storms associated with the nearby passage of hurricanes will also lead to beach erosion. In both cases foreshore recovery likely takes places within a few months after the erosional event (Carter, 1986 and references therein).

The GPR data show that each beach ridge in the study area likely starts as a wave-built swash bar, formed over a period of 7 - 19 years. Once stabilised and no longer subject to hydrodynamic processes, subsequent wind processes create an aeolian cap on the ridge. Sand is blown in from the adjacent beach, including the active intertidal swash bar (exposed during low tide). It is trapped by pioneer vegetation, especially *Ipomoea pes-caprae*, that rapidly colonises the young ridge. The final ridge elevation is determined by the length of the period that the ridge is located next to the beach: the longer the ridge is exposed to aeolian sand deposition, the higher it becomes, also found at other coastal sites (e.g. Shepherd, 1991; cited by Tamura, 2012) Consequently, high beach ridges arise when coastal propagation rate is low. Along individual beach ridges, sections formed relatively close to an active river apex, where progradation rates are high (Fig. 11b), are lower than those formed farther away (Fig. 11c), where progradation rates are low. Apparently, reduced sediment supply leads to higher ridges.

5.2 Beach-ridge elevation as a proxy of riverine sediment supply

Beach-ridge elevation is negatively correlated with progradation rate, both in shore-normal (Transect A, Phase 3A, Fig. 4c) and in a longshore direction (Fig. 11c). For periods when rivers supplied most of the sediment stored in the beach-ridge system, we hypothesise that ridge elevation along shore-normal transects may be used as a proxy of fluvial sediment supply through time and space. Owing to the large storage capacity within the river basin, sediment availability for fluvial transport is not a limiting factor. Peak river-discharge events and extended periods of large supply translate into high progradation rates and lower ridges. Periods of reduced supply during dry conditions, when rivers are less capable of transporting large amounts of sand, result in higher ridges. Evidence for our hypothesis is provided by a comparison of the beach-ridge morphology with independent information on climate in the catchments. During phase 3A relatively high beach ridges were formed along bothTransects A, B and C during the period between 810 – 950 CE (Fig. 10). This period, associated with the Maya Classic collapse, is well known for the occurrence of multiple prolonged droughts in southern Mexico (cf. Hodell et al., 1995) and Guatemala (cf. Wahl et al., 2014).

Direct sediment supply by rivers, however, is not always the main driver in coastal progradation. Cannibalisation of abandoned promontories may generate abundant sandy sediment for anomalously high sediment supply along the downdrift beach. A drastic increase in sediment supply due to the erosion of the SP y SP promontory after the avulsion of the Usumacinta River around 1050 CE resulted in increased availability of sand for aeolian reworking, triggering the formation of relatively high beach ridges on both sites of the eroding SP y SP promontory (Figs. 4b and 10). Even ~1000 years after the avulsion that caused the Usumacinta River to join the Grijalva River at Tres Brazos, coastal erosion at its former SP y SP apex is still ongoing. This process is obscuring the relationship between direct fluvial sediment supply and beach-ridge elevation, but can be recognised as a separate force because it caused major changes in geometry and orientation of beach ridges (Fig. 2a), as well as clear changes in grain-size characteristics (Figs. 4b and 5b).

Detecting changes in fluvial sediment supply from beach ridge elevation differences requires that there are no major changes in wave and wind climate affection the signal. Such changes in wave and wind climate should be reflected in significant changes in the granulometric parameters of the deposited beach ridge sand. After normalising for the effects of new river-mouth initiation and old promontory abandonment, we find only minor remaining granulometric differences in our study area. Comparison of modern deposits to the fossil beach deposits of Transect A (Fig. B3) suggests that wind and wave climate (multi-decadal averaged) during the past 2000 years (Phase 3) have been comparable to those of the present. In contrast, the different geometry of the beach-ridge plain formed during the earlier Phase 2 (Fig. 11a) indicates that wind and wave climate at that time were likely different from the situation today. During Phase 2, progradation rates decreased relatively slowly with increasing distances from the SP y SP River mouth (Fig. 11b), and the promontory seems less asymmetric than the promontory formed during Phase 3C at the joint outlet of the Usumacinta and Grijalva Rivers. This difference can be explained by a higher contribution of high-angle waves from the west in the construction of the delta promontory, especially over the past 500 years, which is in agreement with model simulations of delta development near river outlets (Ashton and Giosan, 2011). Such geometric changes can thus occur without changes in sediment supply.
We speculate that the increased contribution of high-angle waves during Phase 3 is a possible response to the increasingly frequent occurrences of north-westerly winds, probably related to a stronger and more frequent contribution of cold fronts than before. During Phase 2, the Intertropical Convergence Zone (ITCZ) was farther northward, and likely associated with stronger north-easterly winds that could have caused the westward increase in aeolian accretion rates during this time period (Fig. 11c).

5.3 Beach-ridge periodicity

Combining the age-distance modelling with the LiDAR-derived beach-ridge morphometrics (Fig. 2a), it is evident that the development of past ridge-swale couplets took between 7 and 19 years (Table 2), and that the time interval for the formation of subsequent ridge-swale couplets decreased with increasing progradation rate (Table 2). This relationship is apparent not only in shore-normal transects marked by variable progradation rates, but also in a shore-parallel direction, with beach ridges merging away from the river mouth supplying the sediment. It corroborates a similar finding of Thompson (1992) for Lake Michigan beach ridges and indicates that an allogenic cause of individual beach-ridge formation (e.g. periodic decimetre-scale lunar or steric sea-level oscillations; Tanner, 1995), is unlikely. In this light, it should be noted that long time series of water-level data from seven tide gauges along the southern Gulf of Mexico (Salas-de-León et al., 2006) do not show any decadal periodicity. The inter-annual amplitude variability is only a few centimetres, an order of magnitude lower than the intra-annual amplitude range of 25 cm between a February low and an October high. We therefore conclude that ridge-swale couplets at the study site are not formed in response to RSL oscillations. This finding agrees with the findings of Tamura (2012) and Moore et al. (2016) that the formation of individual ridge/swale couplets is driven by autocyclic processes (Moore et al., 2016).
Comparison with periodicities reported from other large beach-ridge systems (Fig. 12) indicates

that low periodicities (< 25 yr) indeed are generally found at sites with high progradation rates (>1.5 m/yr).

6 Conclusions

Our study demonstrates the importance of riverine sediment supply in the formation of the Usumacinta-Grijalva beach-ridge sequence, corroborating earlier geomorphological studies (Psuty, 1965, 1967; West et al., 1969). In contrast to this earlier work, we propose a mechanism of ridge formation without a significant role of storm surges and over-wash deposits. The fine sandy beach ridges were mainly swash built, have an aeolian cap, and likely formed under fair-weather conditions without the requirement of sea-level oscillation. Autocyclic processes controlled the periodicity (7-19 yrs) in beach ridge formation. The relatively low periodicities are related to high progradation rates (> ~1.5 m/yr) and reflect ample sediment supply. The indicative meaning of beach-ridge periodicities in palaeoenvironmental reconstructions is limited.

We estimate that sediment supply, distributed along 150 km of coastline, was roughly 2.3 – 3.5 million m^3/yr, which is exceptionally large compared to that of other large beach-ridge sequences. This can be attributed to extensive availability of easily erodible Los Chocoyos ignimbrites in the headwater catchments of the Usumacinta River, given the abundance of fragmented volcanic material derived from this unit in the beach ridge sands.

Our observations enabled us to subdivide the three main phases in the development of the beach-ridge plain (Psuty, 1965, 1967; West et al., 1969) further into six sub-units, related to changes in the configuration of the main river distributaries of the Usumacinta and Grijalva River system. Combined ^{14}C and OLS dating provided a robust and consistent chronological framework for these phases, which substantially improved the existing chronology based on radiocarbon-dated shell material (Aguayo et al., 1999).

Our analyses show that during periods when the Usumacinta River was the main supplier of sandy sediments to the coast, changes in river discharge determined sediment availability, progradation rate, and the final elevation of the beach ridges. Since the river discharge is directly related to rainfall in the river catchment, beach ridge elevation may be an excellent proxy for temporal changes in regional-scale precipitation.

Acknowledgements

We thank INEGI, Mexico for the generous provision of the LiDAR data, and Hector V. Cabadas-Báez for kindly supplying the major-element data of glass shards recovered from levee deposits at Tierra Blanca. Elise van Winden, Jesse Hennekam and Ryan Nagelkirk provided field support and Salomon Kroonenberg offered valuable advice. We thank the reviewers E. Otvos and T. Tamura for their constructive comments that helped to improve the quality of the paper. This research is supported by the Netherlands Organisation for Scientific Research (NWO grant 821.01.007). Remke van Dam acknowledges support from the Michigan Space Grant Consortium.

References

Aagaard, T., Davidson-Arnott, R., Greenwood, B., and Nielsen, J.: Sediment supply from shoreface to dunes: linking sediment transport measurements and long-term morphological evolution, Geomorphology, 60, 205-224, 2004.

Administración Portuaria Integral de Dos Bocas S.A. de C.V.: Manifestación de Impacto Ambiental Modalidad Particular; Construcción de Escolleras y del Dragado del Canal de Acceso del Puerto de Frontera, Tabasco. Administración Portuaria Integral de Dos Bocas S.A. de C.V., Paraíso, Tabasco, México, 258 pp., 2005.

Aguayo, J.E., Gutiérrez-Estrada, M.A., Araujo-Mendieta, J., Sandoval-Ochoa, J.H., and Vázquez-Gutiérrez, F.: Geodinámica Holocénica y reciente del sistema fluvio deltáico Grijalva-Usumacinta, suroeste del Golfo de México. Revista de la Sociedad Mexicana de Historia Natural 49, 29-44, 1999.

Aitken, M.J., 1998: An Introduction to Optical Dating: The Dating of Quaternary Sediments by the Use of Photon-Stimulated Luminescence, Oxford, Oxford University Press, 267 pp., 1998.

Ashton, A.D., and Giosan, L.: Wave-angle control of delta evolution, Geophysical Research Letters, 38, L13405, 2011.

Ayala-Castañares, A. and Guttiérrez-Estrada, M.: Morfología y sedimentos superficiales de la plataforma continental frente a Tabasco y Campeche, México, Anales del Instituto de Ciencias del Mar y Limnología, UNAM, 17, 163–190, 1990.

Ballarini, M., Wallinga, J., Murray, A.S., Van Heteren, S., Oost, A.P., Bos, A.J.J., and Van Eijk, C.W.E.: Optical dating of young coastal dunes on a decadal time scale, Quaternary Science Reviews, 22(10–13), 1011–1017, 2003.

Balsillie, J.H.: William F. Tanner on Environmental Clastic Granulometry, Special Publication 40, Tallahassee, Florida Geological Survey. 145 pp., 1995.

Banco Nacional de Datos de Aguas Superficiales
http://www.conagua.gob.mx/CONAGUA07/Contenido/Documentos/Portada BANDAS.htm
conagua.gob.mx/Bandas/Bases_Datos_Presas/

Blott, S.J, and Pye, K.: Gradistat: A grain size distribution and statistics package for the analysis of unconsolidated sediments, Earth Surface Processes and Landforms 26, 1237-1248, 2001.

Blum, M.D., Sivers, A.E., Zayac, T., and Goble, R.J.: Middle Holocene Sea-Level and Evolution of the Gulf of Mexico Coast. Gulf Coast Association of Geological Societies Transactions, 53, 64-77, 2003.

Bøtter-Jensen, L., Andersen, C.E., Duller, G.A.T., and Murray, A.S.: Developments in radiation, stimulation and observation facilities in luminescence measurement, Radiation Measurements, 37, 535–541, 2003.

Bristow, C.S., and Pucillo, K.: Quantifying rates of coastal progradation from sediment volume using GPR and OSL: the Holocene fill of Guichen Bay, south-east South Australia, Sedimentology, 53, 769–788, 2006.

Bronk Ramsey, C.: Bayesian analysis of radiocarbon Dates, Radiocarbon, 51, 337–360, 2009.

Bronk Ramsey, C.: Oxcal 4.2., http://c14.arch.ox.ac.uk/oxcal.html, 2016.

Brooke, B., Ryan, D., Pietsch, T., Olley, J., Douglas, G., Packett, R., Radke, L., and Flood, P.: Influence of climate fluctuations and changes in catchment land use on Late Holocene and modern beach-ridge sedimentation on a tropical macrotidal coast: Keppel Bay, Queensland, Australia, Marine Geology, 251, 195–208, 2008a.

Brooke, B., Lee, R., Cox, M., Olley, J., and Pietsch, T.: Rates of Shoreline Progradation during the Last 1700 Years at Beachmere, Southeastern Queensland, Australia, Based on Optically Stimulated Luminescence Dating of Beach Ridges, Journal of Coastal Research, 24, 640–648, 2008b.

Cabadas-Báez, H.V., Solís-Castillo, B., Solleiro-Rebolledo, E., Sedov, S., Leonard, D., and Teranishi-Castillo, K.: Reworked volcaniclastic deposits from the Usumacinta river, Mexico: A serendipitous source of volcanic glass in Maya ceramics, Geoarchaeology, in press.

Carter, R.W.G.: The morphodynamics of beach-ridge formation: Magilligan, Northern Ireland, Marine Geology, 73, 191-214, 1986.

Castillo, S., Pompa, J., and Moreno-Casasola, P.: Coastal sand dune vegetation of Tabasco and Campeche, Mexico. Journal of Vegetation Science, 2, 73-88, 1991.

Cleveringa, J.: Reconstruction and modelling of Holocene coastal evolution of the western Netherlands, PhD thesis Utrecht University, the Netherlands, 2000.

Cunningham, A.C., and Wallinga, J.: Realizing the potential of fluvial archives using robust OSL chronologies, Quaternary Geochronology, 12, 98-106, 2012.

Cunningham, A.C., and Wallinga, J.: Selection of integration time-intervals for quartz OSL decay curves, Quaternary Geochronology, 5, 657-666, 2010.

Curray, J.R., Emmel, F.J., and Crampton, P.J.S.: Holocene history of a strand plain, lagoonal coast, Nayarit, Mexico. In: Ayala-Casteñares, A., Phleger, F.B. (Eds.), Lagunas Costeras, UN Symposium. UNAM-UNESCO, Mexico, D.F, 63–100, 1969.

Dogan, M., Van Dam, R.L., Bohling, G.C., Butler, J.J., and Hyndman, D.W.: Hydrostratigraphic analysis of the MADE site with full-resolution GPR and direct-push hydraulic profiling, Geophysical Research Letters, 38, L06405, 2011.

Donnelly, J.P. and Giosan, L.: Tempestuous highs and lows in the Gulf of Mexico, Geology, 36, 751-752, 2008.

Drexler, J.W., Rose, W.I., Sparks, R.S.J., and Ledbetters, M.T.: The Los Chocoyos Ash, Guatemala: A major stratigraphic marker in middle America and in three ocean basins, Quaternary Research, 13, 327–345, 1980.

Duller, G.A.T.: Distinguishing quartz and feldspar in single grain luminescence measurements, Radiation Measurements, 37, 161–165, 2003.

FitzGerald, D.M., Buynevich, I.V., Fenster, M.S., and McKinlay, P.A.: Sand dynamics at the mouth of a rock-bound, tide-dominated estuary, Sedimentary Geology, 131, 25-49, 2000.

Folk R.L., and Ward, W.C.: Brazos River bar: a study in the significance of grain size parameters, Journal of Sedimentary Petrology, 27, 3–26, 1957.

Forrest, B.M.: Evolution of the Beach Ridge Strandplain on St. Vincent Island, Florida, Thesis, Florida State University, 269 pp., 2007.

Forsyth, A.J., Nott, J., and Bateman, M.D., Beach ridge plain evidence of a variable late-Holocene tropical cyclone climate, North Queensland, Australia, Palaeogeography, Palaeoclimatology, Palaeoecology, 297, 707–716, 2010.

Galbraith, R.F., Roberts, R.G., Laslett, G.M., Yoshida, H., and Olley, J.M.: Optical dating of single and multiple grains of quartz from Jinmium rock shelter, Northern Australia: part I, experimental design and statistical models, Archaeometry, 41, 339–364, 1999.

Gallego-Fernández, J.B., and Martínez, M.L.: Environmental filtering and plant functional types on Mexican foredunes along the Gulf of Mexico. Ecoscience, 18(1), 52-62, 2011.

Garrison Jr., J.R., Mestas-Nuñez, A.M., Williams, J.R., and Lumb, L.M.: Can beach dune ridges of the Texas Gulf Coast preserve climate signals?, Geo-Mar. Lett., 32, 241–250, 2012.

Garrity, C.P., and Soller, D.R.: Database of the Geologic Map of North America; adapted from the map by J.C. Reed, Jr. and others (2005): U.S. Geological Survey Data Series 424 [https://pubs.usgs.gov/ds/424/], 2009.

Gischler, E., and Hudson, J.H.: Holocene development of the Belize barrier reef, Sediment. Geol., 164, 223-236, 2004.

Guedes, C.C.F., Giannini, P.C.F., Nascimento Jr., D.R. Sawakuchi, A.O., Tanaka, A.P.B., and Rossi, M.G.: Controls of heavy minerals and grain size in a holocene regressive barrier (Ilha Comprida, southeastern Brazil), Journal of South American Earth Sciences, 31, 110-123, 2011.

Guérin, G., Mercier, N., and Adamiec, G.: Dose-rate conversion factors: update: Ancient TL, 29, 5-8, 2011.

Harp, E.L., Wilson, R.C., Wieczorek, G.F.: Landslides from the February 4, 1976, Guatemala earthquake, US Geological Survey, Prof. Paper 1024-A, 1981.

Hijmans, R.J., Cameron, S.E., Parra, J.L., Jones, P.G., and Jarvis, A.:Very high resolution interpolated climate surfaces for global land areas. International Journal of Climatology, 25, 1965-1978, 2005.

Hinojosa, C., Nooren, K., Solleiro-Rebolledo, E., Sedov, S., Salazar, O.: Soil development on a beach ridge chronosequence in the Gulf of Mexico coastal plain and its relation to the ancient land use, Quaternary International, 418, 180-194, 2016.

Hodell, D.A., Curtis, J.H., and Brenner, M.: Possible role of climate in the collapse of Classic Maya civilization, Nature, 375(6530), 391–394, 1995.

Instituto Geográfico Nacional: Mapa Geológico de Guatemala a escala 1:500,000, 1970.

Jol, H.M., Smith, D.G., and Meyers, R.A.: Digital ground penetrating radar (GPR): a new geophysical tool for coastal barrier research (examples from the Atlantic, Gulf and Pacific Coasts, U.S.A.), Journal of Coastal Research, 12, 960–968, 1996.

Jom Morán, S.A.: Medición batimétrica para determinar el volumen de material sedimentado acumulado durante el tiempo de servicio del embalse Pueblo Viejo, de la central hidroeléctrica Chixoy. Msc thesis, Universidad de San Carlos de Guatemala, 2010.

Keijsers, J.G.S., Poortinga, A., Riksen, M.J.P.M., and Maroulis, J.: Spatio-Temporal Variability in Accretion and Erosion of Coastal Foredunes in the Netherlands: Regional Climate and Local Topography. PLoS ONE 9(3), e91115, doi:10.1371/journal.pone.0091115, 2014.

Koch, A.J., and McLean, H.: Pleistocene tephra and ash-flow deposits in the volcanic highlands of Guatemala. Geological Society of America Bulletin, 86, 529-541, 1975.

Komar, P.D.: The entrainment, transport and sorting of heavy minerals by waves and currents, Developments in Sedimentology, 58, 3–48, 2007.

Kossin, J.P., Camargo, S.J., and Sitkowski, M.: Climate modulation of North Atlantic Hurricane tracks, Journal of Climate 23, 3057-3076, 2010.

Kutterolf, S., Freundt, A., Peréz, W., Mörz, T., Schacht, U., Wehrmann, H., and Schmincke, H.-U.: Pacific offshore record of plinian arc volcanism in Central America: 1. Along-arc correlations: Geochemistry, Geophysics, Geosystems, 9, Q02S01, 2008.

López, G.I., and Rink, W.J.: New quartz optical stimulated luminescence ages for beach ridges on the St. Vincent Island Holocene strand plain, Florida, United States. Journal of Coastal Research, 24, 49–62, 2008.

Marrufo, R.J., and González, F.J.: Use of Lidar Data in Floodplain Risk Management Planning: The Experience of Tabasco 2007 Flood. In Advances in Geoscience and Remote Sensing, INTECH, chapter 32, 659-678, 2012.

May, J.H., Wells, S.G., Cohen, T.J., Marx, S.K., Nanson, G.C., and Baker, S.E.: A soil chronosequence on Lake Mega-Frome beach ridges and its implications for late Quaternary pedogenesis and paleoenvironmental conditions in the drylands of southern Australia, Quaternary Research, 83, 150-165, 2015.

McCave, I.N.: Grain-size trends and transport along beaches: example from eastern England. Marine Geology, 28, M43-M51, 1978.

Milana, J.P., Conforti Ferreira Guedes, C., and Valdez Buso, V.: The coastal ridge sequence at Rio Grande do Sul: A new geoarchive for past climate events of the Atlantic coast of southern Brazil since the mid Holocene, Quaternary International, in press.

Milliken, K.T., Anderson, J.B., and Rodriguez, A.B.: A new composite Holocene sea-level curve for the northern Gulf of Mexico, The Geological Society of America, Special Paper 443, 1-11, 2008.

Minderhoud, P., Cohen, K.M., Toonen, W.H.J., Erkens, G., and Hoek, W.Z.: Improving age-depth models of fluvio-lacustrine deposits using sedimentary proxies for accumulation rates, Quaternary Geochronology, 33, 35-45, 2016.

Mook, W.G., and Van der Plicht, J.: Reporting ^{14}C activities and concentrations, Radiocarbon, 41, 227-239, 1999.

Moore, L.J., Durán Vinent, O., and Ruggiero, P.: Vegetation control allows autocyclic formation of multiple dunes on prograding coasts, Geology, 44(7), 559–562, 2016.

Morton, R.A., Paine, J.G., and Blum, M.D.: Responses of stable bay-margin and barrier-island systems to Holocene sea-level highstands, western Gulf of Mexico, Journal of Sedimentary Research, 70, 478–490, 2000.

Muñoz-Salinas, E. Castillo, M., Sanderson, D., Kinnaird, T., and Cruz-Zaragoza, E.: Using three different approaches of OSL for the study of young fluvial sediments at the coastal plain of the Usumacinta–Grijalva River Basin, southern Mexico, Earth Surface Processes and Landforms, 41, 823–834, 2016.

Murray-Wallace, C.V., Banerjee, D., Bourman, R.P., Olley, J.M. and Brooke, B.P.: Optically stimulated luminescence dating of Holocene relict foredunes, Guichen Bay, South Australia, Quaternary Science Reviews, 21, 1077-1086, 2002.

Murray, A.S., and Wintle, A.G.: The single aliquot regenerative dose protocol: potential for improvements in reliability. Radiation Measurements, 37, 377-381, 2003.

Neal, A.: Ground-penetrating radar and its use in sedimentology: principles, problems and progress, Earth-Science Reviews, 66, 261-330, 2004.

Nielsen, A., Murray, A.S., Pejrup, M., and Elberling, B.: Optically stimulated luminescence dating of a Holocene beach ridge plain in Northern Jutland, Denmark, Quaternary Geochronology, 1, 305–312, 2006.

Nielsen, A.H., Elberling, B., and Pejrup, M.: Soil development rates from an optically stimulated luminescence-dated beach ridge sequence in Northern Jutland, Denmark, Canadian Journal of Soil Science, 90(2), 295-307, 2010.

Nieuwenhuyse, A., and Kroonenberg, S.B.: Volcanic origin of Holocene beach ridges along the Caribbean coast of Costa Rica, Marine Geology, 120, 13–26, 1994.

Nooren, K., Hoek, W.Z., Van der Plicht, H., Sigl, M., Van Bergen, M.J., Galop, D., Torrescano-Valle, N., Islebe, G., Huizinga, A., Winkels, T., and Middelkoop, H.: Explosive eruption of El Chichón volcano (Mexico) disrupted 6th century Maya civilization and contributed to global cooling, Geology, 45(2), 175-178, 2017.

Nott, J., Smithers, S., Walsh, K., Rhodes, E.: Sand beach ridges record 6000 year history of extreme tropical cyclone activity in northeastern Australia, Quaternary Science Reviews, 28, 1511–1520, 2009.

Nott, J.: A 6000 year tropical cyclone record from Western Australia, Quaternary Science Reviews, 30, 713–722, 2011.

Oliver, T.S.N.: Holocene depositional history of three coastal sand ridge plains, southeastern Australia. Doctor of Philosophy thesis, School of Earth and Environmental Sciences, University of Wollongong, Australia, 216 pp., 2016.

Oliver, T.S.N., Dougherty, A.J., Gliganic, L.A., and Woodroffe, C.D.: Towards more robust chronologies of coastal progradation: optically stimulated luminescence ages for the coastal plain at Moruya, south-eastern Australia, The Holocene, 25, 536–546, 2015.

Ollerhead, J., Davidson-Arnott, R., Walker, I.J., and Mathew, S.: Annual to decadal morphodynamics of the foredune system at Greenwich Dunes, Prince Edward Island, Canada, Earth Surface Processes and Landforms, 38, 284-298, 2013.

Ortíz-Pérez, M.A.: Retroceso reciente de la línea ed costa del frente deltáico del Río San Pedro, Campeche-Tabasco, Investigaciones Geográficas, 25, 7-24, 1992.

Ortíz-Pérez, M.A., Hernández-Santana, J.R., Figueroa Mah Eng, J.M., and Gama Campillo, L.: Tasas del avance transgresivo y regresivo en el frente deltaico tabasqueño: en el período comprendido del año 1995 al 2008. In: Vulnerabilidad en las zonas costeras mexicanas ante el cambio climático, Botello, A.V., Villanueva-Fragoso, S., Gutiérrez, J., and Rojas Galaviz, J.L. (eds.), UNAM-INE, 305-324, 2010.

Otvos, E.G.: Beach Ridges — definitions and significance, Geomorphology, 32, 83–108, 2000.

Otvos, E.G.: Coastal barriers, Gulf of Mexico: Holocene evolution and chronology, Journal of Coastal Research, SI(42), 141-163, 2005.

Padilla, R.J., and Sánchez: Evolución geológica del sureste mexicano desde el Mesozoico al presente en el contexto regional del Golfo de México, Boletín de la Sociedad Geológica Mexicana, Tomo LIX(1), 19-42, 2007.

Pietsch, T.J., Olley, J.M., and Nanson, G.C.: Fluvial transport as a natural luminescence sensitiser of quartz, Quaternary Geochronology 3, 365-376, 2008.

Prescott, J.R., and Hutton, J.T.: Cosmic ray distributions to dose rates for luminescence and ESR dating: large depths and long-term variations, Radiation Measurements, 23, 497–500, 1994.

Psuty, N.P.: Beach ridge development in Tabasco, Mexico, Annals Association of American Geographers, 55, 112–124, 1965.

Psuty, N.P.: The Geomorphology of Beach Ridges in Tabasco, Mexico, Coastal Studies Series 18, Louisiana State University Press, Baton Rouge, USA, 51 pp., 1967.

Ramos J., Marrufo L., and González F.J.: Use of Lidar Data in Floodplain Risk Management Planning: The Experience of Tabasco 2007 Flood In: Jedlovec, G. (ed.), Advances in Geoscience and Remote Sensing, Intech, doi: 10.5772/8322, 2009.

Reimann, T., Tsukamoto, S., Harff, J., Osadczuk, K., and Frechen, M.: Reconstruction of Holocene coastal foredune progradation using luminescence dating — An example from the Świna barrier (southern Baltic Sea, NW Poland), Geomorphology, 132, 1–16, 2011.

Reimer, P.J., et al.: IntCal13 and Marine13 radiocarbon age calibration curves 0–50,000 years cal BP, Radiocarbon, 55, 1869–1887, 2013.

Remillard, A.M., Buylaert, J.-P., Murray, A.S., St-Onge, G., Bernatches, P., and Hetu, B.: Quartz OSL dating of the late Holocene beach ridge from the Magdalen Islands (Quebec, Canada), Quaternary Geochronology, 30, 264-269, 2015.

Rink, W.J. and López, G.I.: OSL-based lateral progradation and aeolian sediment accumulation rates for the Apalachicola Barrier Island Complex, North Gulf of Mexico, Florida, Geomorphology, 123, 330-342, 2010.

Rose, W.I., Newhall, C.G., Bornhorst, T.J., Self, C.: Quaternary silicic pyroclastic deposits of Atitlán Caldera, Guatemala, Journal of Volcanology and Geothermal Research, 33, 57-80, 1987.

Salas-de-León, D.A., Monreal-Gómez, M.A., Salas-Monreal, D., Riverón-Enzástiga, M.L., and Sánchez-Santillan, N.L.: Inter-annual sea level variability in the southern Gulf of Mexico (1966–1976), Geophysical Research Letters, 33, L08610, 2006.

Salas-de-León, D.A., Monreal-Gómez, M.A., Miguel Díaz-Flores, M.A., Salas-Monreal, D., Velasco-Mendoza, H., Riverón-Enzástiga, M.L., and Ortiz-Zamora, G.: Role of Near-Bottom Currents in the Distribution of Sediments within the Southern Bay of Campeche, Gulf of Mexico, Journal of Coastal Research, 24(6), 1487–1494, 2008.

Sánchez-Núñez, M.M., Macías, J.L., Saucedo, R., Zamorano, J.J., Novelo, D., Mendoza, M.E., and Torres-Hernández, J.R.: Geomorphology, internal structure and evolution of alluvial fans at Motozintla, Chiapas, Mexico, Geomorphology, 230, 1-12, 2015.

Scheffers, A., Engel, M., Scheffers, S., Squire, P., Kelletat, D.: Beach ridge systems – archives for Holocene coastal events?, Progress in Physical Geography, 36(1), 5–37, 2012.

Shepherd, M.J.: Relict and contemporary foredunes as indicators of coastal processes. In: Applied Quaternary Studies. Brierley, G., and Chappell, J. (eds.), Australian National University, Canberra, Australia, 17–24, 1991.

Solís-Castillo, B., Thiel, C., Cabadas-Báez, H., Solleiro-Rebolledo, E., Sedov, S., Terhorst, B., Damm, B., Frechen, M., and Tsukamoto, S.: Holocene sequences in the Mayan Lowlands—A provenance study using heavy mineral distributions. Eiszeitalter und Gegenwart Quaternary Science Journal, 62, 84–97, 2013.

Stapor, F.W., Jr., Mathews, T.D., and Lindfors-Kearns, F.E.: Barrier-island progradation and Holocene sealevel history in southwest Florida, Journal of Coastal Research, 7, 815–838, 1991.

Tamura, T.: Beach ridges and prograded beach deposits as palaeoenvironment records, Earth-Science Reviews, 114, 279-297, 2012.

Tamura, T., Murakami, F., and Watanabe, K.: Holocene beach deposits for assessing coastal uplift of the northeastern Boso Peninsula, Pacific coast of Japan, Quaternary Research, 74, 227–234, 2010.

Tanner, W.F.: Origin of beach ridges and swales. Marine Geology, 129, 149–161, 1995.

Tanner, W.F.: Late Holocene sea-level changes from grain-size data: evidence from the Gulf of Mexico, The Holocene, 2, 249–254, 1992.

Taylor, M.J., and Stone, G.W.: Beach-ridges: a review, Journal of Coastal Research, 12, 612–621, 1996.

Thompson, T.A.: Beach-ridge development and lake-level variation in southern Lake Michigan, Sedimentary Geology, 80, 305–318, 1992.

Törnqvist, T.E., Gonzalez, J.L., Newsom, L.A., van der Borg., K., de Jong, A.F.M., and Kurnik, C.W.: Deciphering Holocene sea-level history on the U.S. Gulf Coast: A high-resolution record from the Mississippi Delta: Geological Society of America Bulletin, 116, 1026–1039, 2004.

Tsukamoto, S., Rink, W.J., and Watanuki, T.: OSL of tephric loess and volcanic quartz in Japan and an alternative procedure for estimating De from a fast OSL component, Radiation measurements 37, 459-465, 2003.

USGS: Shuttle Radar Topography Mission (SRTM) 1 Arc-Second Global dataset, https://lta.cr.usgs.gov/SRTM1Arc, 2009.

Van Dam, R.L.: Landform characterization using geophysics - Recent advances, applications, and emerging tools, Geomorphology, 137, 57-73, 2012.

Van Dam, R.L., and Schlager, W.: Identifying causes of ground-penetrating radar reflections using time-domain reflectometry and sedimentological analyses, Sedimentology, 47, 435-449, 2000.

Van der Meene, E.A., Van der Staay, J., and Lay Hock, T.: The Van der Staay suction-corer – a simple apparatus for drilling in sand below groundwater table, Rijks Geologische Dienst, Haarlem, the Netherlands, 1979.

Van der Plicht, J., Wijma, S., Aerts, A.T., Pertuisot, M.H., and Meijer, H.A.J.: The Groningen AMS facility: status report, Nuclear Instruments and Methods, B172, 58-65, 2000.

Van Heteren, S., Fitzgerald, D.M., Mckinlay, P.A., and Buynevich, I.V.: Radar facies of paraglacial barrier systems: coastal New England, USA, Sedimentology, 45(1), 181–200, 1998.

Van Overmeeren, R.A.: Radar facies of unconsolidated sediments in the Netherlands: A radar stratigraphy interpretation method for hydrogeology, Journal of Applied Geophysics, 40, 1-18, 1998.

Vespremeanu-Stroe, A., Preoteasa, L., Zăinescu, F., Rotaru, S., Croitoru, L., and Timar-Gabor, A.: Formation of Danube delta beach ridge plains and signatures in morphology, Quaternary International, 415, 268-285, 2016.

Von Nagy, C.: Of Meandering Rivers and Shifting Towns: Landscape Evolution and Community within the Grijalva delta. PhD thesis, Tulane University, USA, 1640 pp., 2003.

Visher, G.S.: Grain size distributions and depositional processes, Journal of Sedimentary Petrology, 39(3), 1074–1106, 1969.

Wahl, D., Byrne, R., and Anderson, L.: An 8700 year paleoclimate reconstruction from the southern Maya lowlands. Quaternary Science Reviews, 103, 19–25, 2014.

Wallinga, J.: Optically stimulated luminescence dating of fluvial deposits: a review, Boreas, 31, 303–322, 2002.

West, R.C., Psuty, N.P., and Thom, B.G.: The Tabasco Lowlands of Southeastern Mexico, Technical Report 70, Louisiana State University, Baton Rouge, USA, 198 pp., 1969.

Figure captions

Figure 1: (a) Location of the Usumacinta-Grijalva beach-ridge sequence (yellow) along the edge of the Holocene delta plain (blue) and the drainage basins of the two main rivers traversing the headlands of this delta (red outlines). Simplified geological map modified from Garrity and Soller (2009) and extent of Los Chocoyos pyroclastic flow deposits adopted from the geological map of Guatemala at scale 1:500,000 (Instituto Geográfico Nacional, 1970; Koch and McLean, 1975; Rose et al.,1987; and Sánchez-Núñez et al., 2015). Elevated uplands above 500 m+MSL, outlined using the SRTM 1-arc-second dataset (USGS, 2009), are depicted in gray; (b) Overview of the Usumacinta-Grijalva delta and the three main phases of Holocene beach-ridge formation defined by Psuty (1965, 1967). The apexes of the two main rivers (yellow dots) are indicated with 25, 50 and 75 km equidistant lines (red lines). Nearshore distribution of coarse silty to gravelly surficial sediments after Ayala-Castañares and Guttiérrez-Estrada (1990). Surficial sediments from the remaining part of the continental shelf are composed of clay and fine silt.

Figure 2: (a) LiDAR-based DEM and location of studied transects, with the GPR transects in blue; (b) Main beach-ridge-formation phases, and locations of sediment cores (black) and of samples collected for OSL and AMS ^{14}C dating. Numbers 1-15 denote the fifteen cross-normal ribbon-shaped elevation transects, in the text referred to as B2-1, B2-2, etc.

Figure 3: Age-distance models for Transects A (a), and B (b). Indicated are the 1 sigma distribution for the model results using the P_sequence module in Oxcal 4.2 (Bronk Ramsey, 2009). Sample locations of AMS ^{14}C (black squares) and OSL (red dots) samples are indicated, and projected samples are presented in italics. The calibrated ^{14}C ages are indicated with the full probability distribution and the OSL ages (red and yellow triangles) with their 1 sigma range. $CaCO_3$ content for selected core samples indicates pedogenic decalcification depth, used to

estimate the position of MSL during beach-ridge formation. The dashed trendline is based on Gischler and Hudson's (2004) reconstruction of late-Holocene RSL.

Figure 4: (a) Core locations along Transect A2; (b) Median grain size of analysed sand samples, with associated shoreface-dipping angle; (c) Age-distance model (after Nooren et al., 2017) and OSL ages (red dots) (with 1 sigma probability).

Figure 5: (a) Reconstructed palaeoshorelines (ages in Year CE); (b) Median grain size (μm) of wave-formed and aeolian deposits (large and small dots, respectively).

Figure 6: (a) Shore-parallel variability in grain-size parameters of swash (red) and aeolian (black) facies. Vfs = very fine sand; fs = fine sand; ms = medium sand; cs = coarse sand.

Figure 7: (a) Grain-size variability along a beach-to-nearshore profile of surficial grab samples taken during fair-weather conditions in April 2013 at Playa Estrella (see Fig. 6 for location). Sand characteristics of beach core 197 (triangle; sample from –3.5 m+MSL), taken in 2012 at the same location are shown for comparison. The sand sample likely had its origin in the nearshore at a distance of 240 - 300 m from the contemporary low-tide line (here shown at 240 m), assuming a comparable beach profile during time of deposition. LWL and HWL are mean low and high water level; (b) Grain-size distribution of representative surficial sand samples from the beach profile, denoted by coloured circles in Fig. 7a.

Figure 8. Processed GPR data and interpretation for two closely spaced relatively elevated beach ridges along Transect A (see Fig. 2a and 3a for location). Time-to-depth conversion for the elevation axis was based on velocities of 0.125 and 0.06 m/ns above and below the water table, respectively. The position of the water table at 0.2 m+MSL (blue dashed line) was drawn on the basis of changes in reflection characteristics, and confirmed by observations from core 72 (black arrow). Here, the water table was positioned at 2.2 m below the land surface. Highlighted in the interpretation are foreshore and shoreface deposits (black dipping lines), and the transition from foreshore to backshore and/or aeolian deposits at 0.8 m+MSL (red dashed line). Also shown are reflection terminations (black half arrows) indicating possible bar welding and some landward-dipping structures (orange lines) possibly related to infill of a large former runnel. The curved reflections around 110 m (40 ns and deeper) are caused by surface scattering off a large nearby tree that was passed while moving the GPR along the transect.

Figure 9: SiO_2 - CaO diagram for analysed volcanic glass shards, plotted along with compositional characteristics of El Chichón (Nooren et al., 2017) and Los Chocoyos tephra (Kutterolf et al., 2008). Data points represent averages for 5-12 particles (bars are 1 sigma). The SiO_2 – CaO composition of volcanic glass shards recovered from Usumacinta levee deposits at Tierra Blanca III (Cabadas-Báez et al., 2017) are indicated for comparison. We refer to table A3 for all major element data. Inset: Thin section of pumice and volcanic glass shards recovered from the beach-ridge sands (core 197, sample from 80 cm below surface). Notice elongated vesicularity of one of the pumice fragments.

Figure 10: Mean beach-ridge elevation variability along shore-normal Transects B (a), A (b) and C (c). See Fig.11a for the location of the individual transects. Notice relatively high beach-ridge elevations around 800-950 CE for all three transect. This period is known for the occurrence of multiple prolonged droughts, and has been related to the Classic Maya collape.

Figure 11: Variability in shore-parallel beach-plain progradation rate (b) and mean elevation (c) for Phase 2 (1800 BCE - 150 CE) (orange/red) and Phase 3C (1460 - 1965 CE) (green). Dashed lines represent calculated elevation values for constant ‘aeolian’ accretion rates. Arrows in panel (a) indicate the estimated dominant direction of swell driving the formation of the swash deposits, and the dominant wind direction related to aeolian sand transport, responsible for the formation of an aeolian cap on top of the swash-built beach ridges.

Figure 12: Periodicities of beach-ridge formation for the Usumacinta-Grijalva (Us-Gr) system compared with reported or estimated values for other large beach-ridge systems: Rockingham Bay (Forsyth et al., 2010), Beachmere (Brooke et al., 2008b), Moruya (Oliver et al., 2015), Guichen Bay (Murray Wallace et al., 2002; Bristow and Pucillo, 2006), Keppel Bay (Brooke et al., 2008a), Shark Bay (Nott, 2011), Cowley beach (Nott et al., 2009), Lake Michigan (Thompson, 1992), St. Vincent Island (Lopez and Rink, 2008; Rink and Lopez, 2010), Jerup (Nielsen et al., 2006), Nayarit (Curray et al., 1969) and Rio Grande do Sul (Milana et al., in press).

Table 1. General characteristics for the watersheds of the main rivers draining towards the Usumacinta-Grijalva delta.

Table 2: General characteristics of the beach-ridge plain along the shore-normal transects as indicated in figure 2A.

Appendix A

Table A1: AMS ^{14}C-dated samples.

Table A2: OSL-dated samples

Table A3: Major-element composition (mean and standard deviation) of volcanic glass and pumice fragments recovered from the beach-ridge sediments along Transect A. Oxide concentrations are normalized to 100% on a volatile-free basis. All iron is taken as FeO. The major-element composition of volcanic glass shards from Tierra Blanca III were generously provided by Hector V. Cabadas-Báez (Cabadas-Báez et al., 2017).

Appendix B

Figure B1: Scour holes along a beach-ridge formed around 1450 CE.

Figure B2: Age-distance scenarios for Transect B2, assuming a constant aeolian accretion rate in a shore-normal direction. The combined calibrated ages for OSL and AMS samples 440 and 433/336 (154 +/-65 and 1720 +/-65 BCE), calculated with Oxcal 4.2 (Bronk Ramsey, 2009) using the IntCal13 calibration curve (Reimer et al., 2013), are used as model boundaries. Indicated are five long-range (red) and five short-range (blue) scenarios for Transect B2-1 – B2-5. The calibrated 1 sigma age range for a P_sequence model solely based on OSL ages (excluding sample 437) is indicated in grey.

Figure B3: Variability in grain-size distribution of sand samples along Transect A at 0.04-14.5 km from the current coastline. Vfs = very fine sand; fs = fine sand; ms = medium sand; cs = coarse sand. Grain-size distributions of representative surficial samples from the current beach profile (Fig. 7c) are indicated for comparison.

Figure B4: Grain size statistical parameters, calculated conform the logarithmic method of moments (Blott and Pye, 1975). Sample locations are indicated in Fig. B3.


(a)
93°W
90°W
Gulf of Mexico
GOM
Caribbean Sea
Pacific Ocean
Sierra
Chilapa
Tierra Blanca
El Chichón
Usumacinta
Grijalva
Chiapas massif
Chixoy dam
Motagua
15°N
Atitlán caldera
0
100 km
hydroelectric dam
volcanoes
Holocene beach ridge plain
Holocene delta plain
Geologic units
Sedimentary
Volcanic
Los Chocoyos ignimbrites
Plutonic
Metamorphic and undivided crystalline

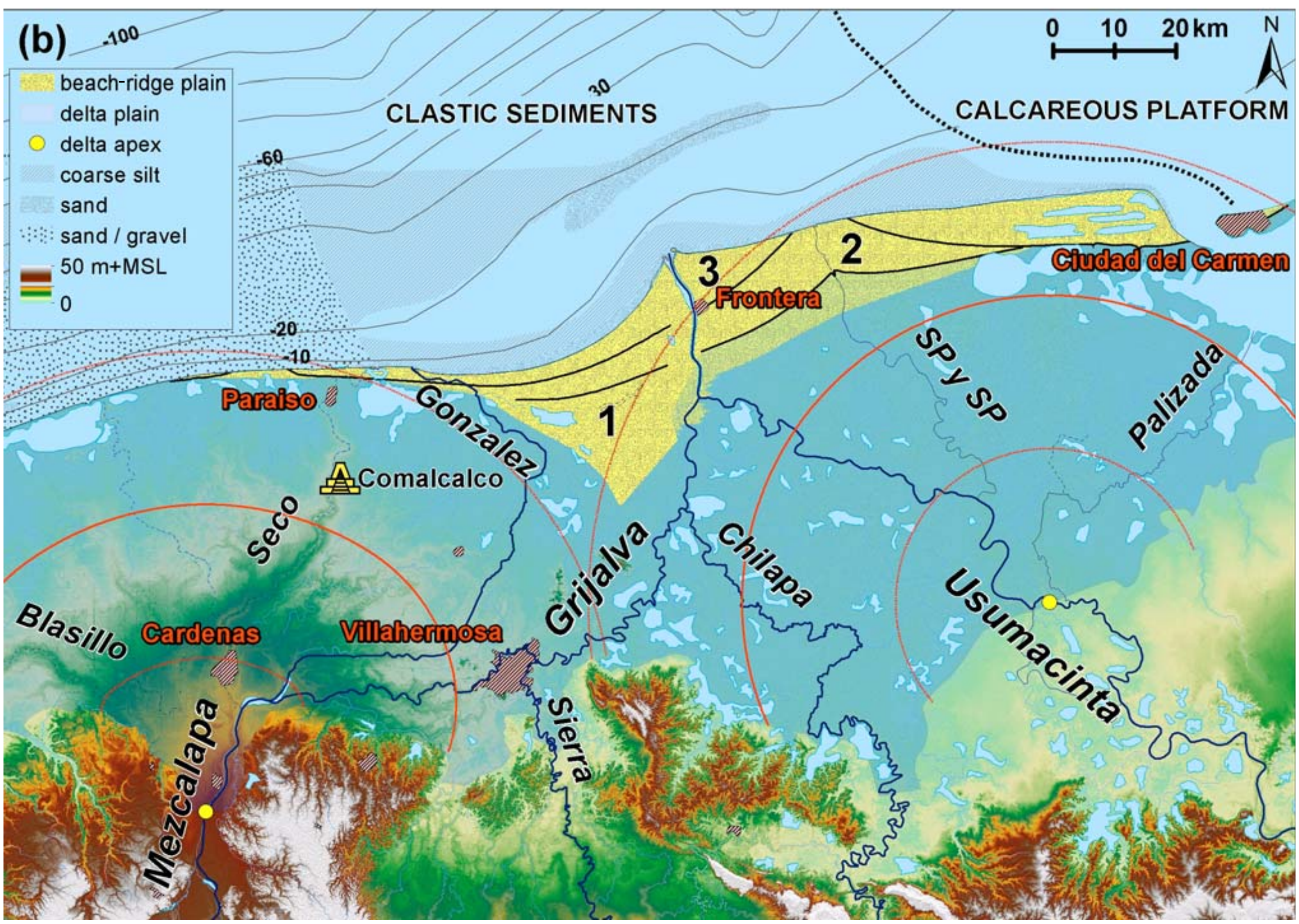
(b)
-100
30
-60
-20
-10
beach-ridge plain
delta plain
delta apex
coarse silt
sand
sand / gravel
50 m+MSL
0
CLASTIC SEDIMENTS
CALCAREOUS PLATFORM
0
10
20 km
Ciudad del Carmen
Frontera
1
2
3
Paraiso
Gonzalez
Comalcalco
SP y SP
Palizada
Seco
Chilapa
Grijalva
Usumacinta
Blasillo
Cardenas
Villahermosa
Sierra
Mezcalapa

Figure 1

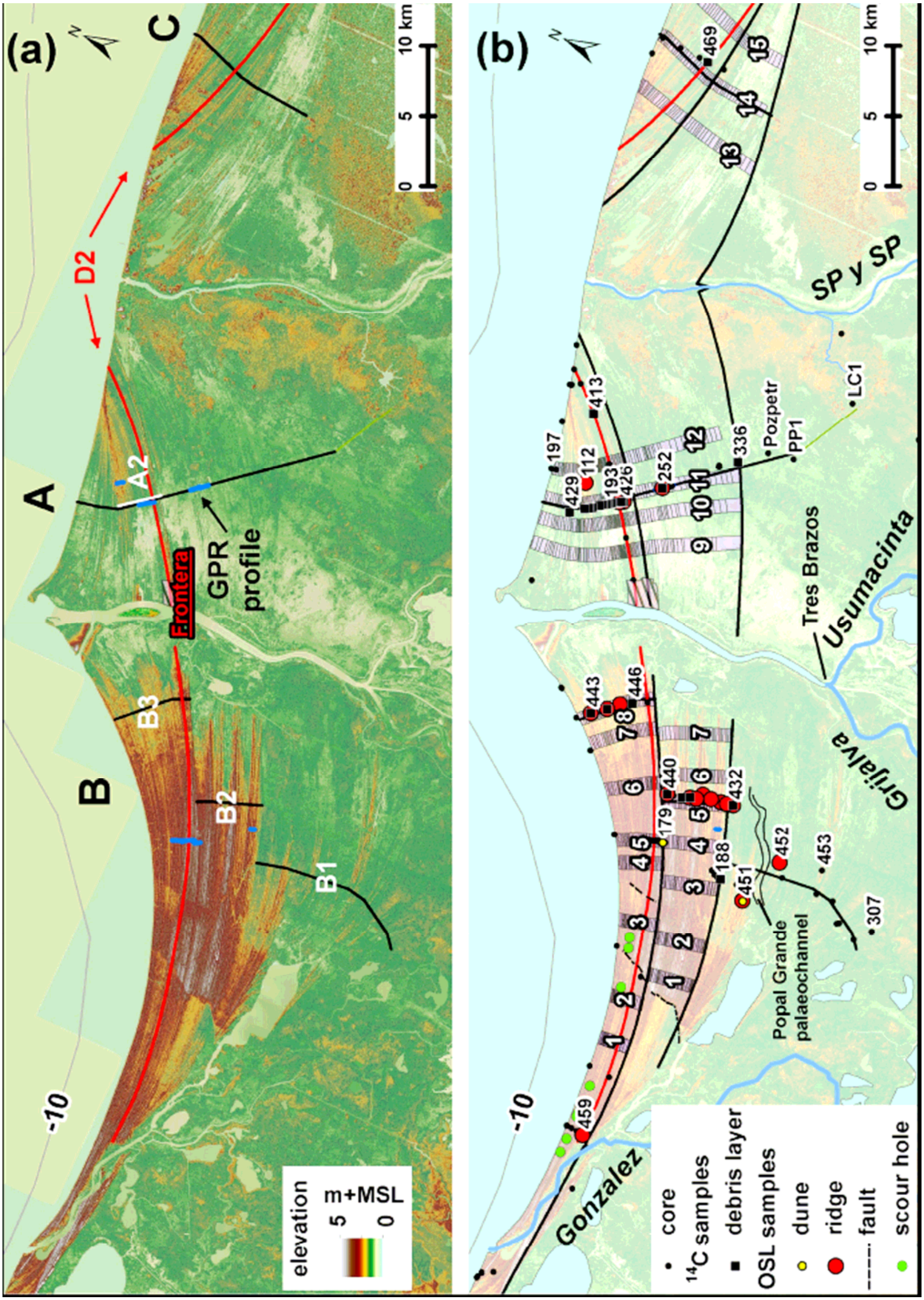

(a)
A
B
C
D2
A2
B1
B2
B3
Frontera
GPR profile
-10
0 5 10 km
elevation
m+MSL
5
0
(b)
Gonzalez
Grijalva
Usumacinta
Tres Brazos
SP y SP
Popal Grande palaeochannel
Pozpetr
PP1
LC1
core
14C samples
debris layer
OSL samples
dune
ridge
fault
scour hole

Figure 2

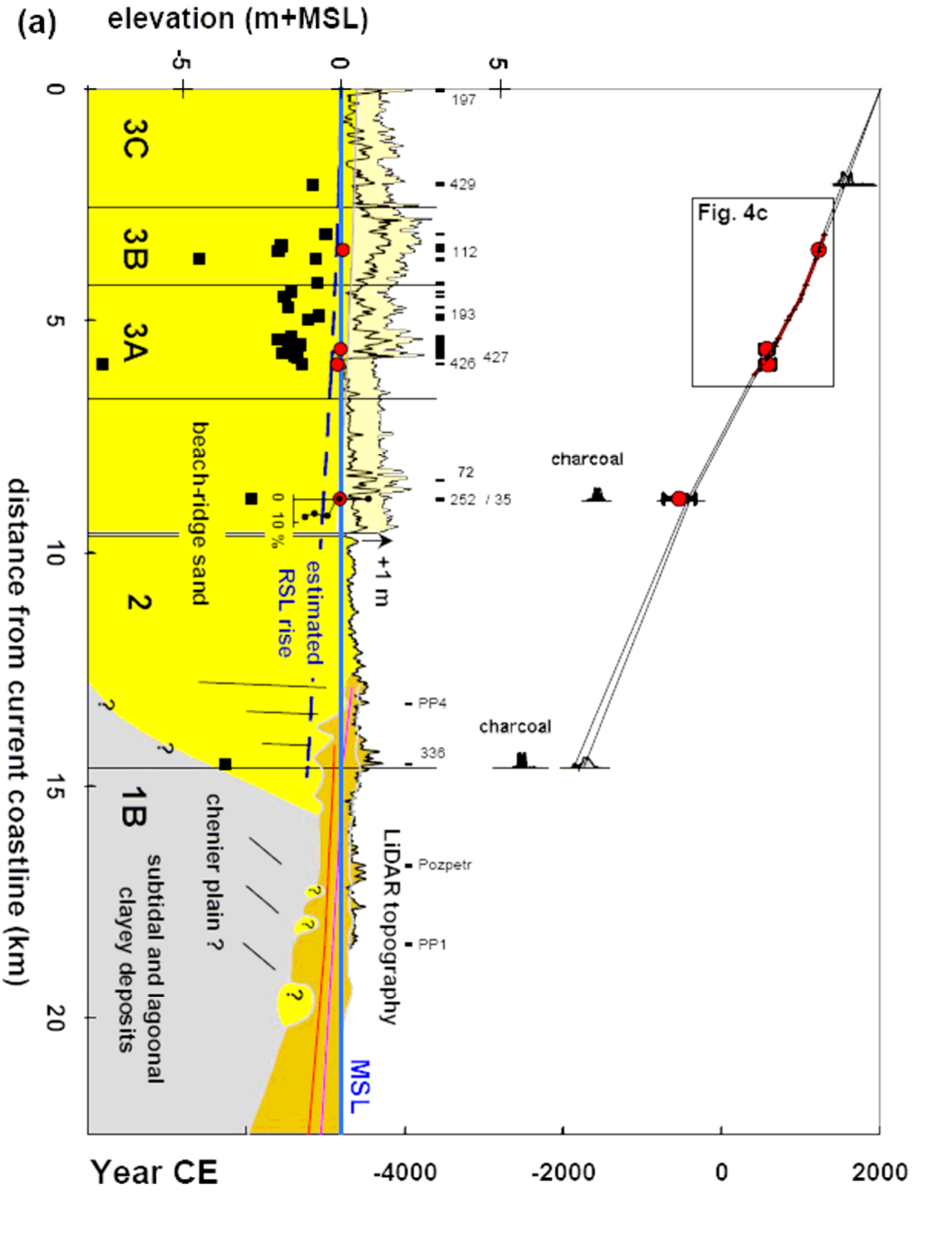
(a)
elevation (m+MSL)
-5
0
5
distance from current coastline (km)
0
5
10
15
20
3C
3B
3A
2
1B
beach-ridge sand
chenier plain ?
subtidal and lagoonal
clayey deposits
estimated
RSL rise
0 10 %
+1 m
LiDAR topography
MSL
197
429
112
193
426
427
72
252 / 35
PP4
336
Pozpetr
PP1
charcoal
charcoal
Fig. 4c
Year CE
-4000
-2000
0
2000

Figure 3a

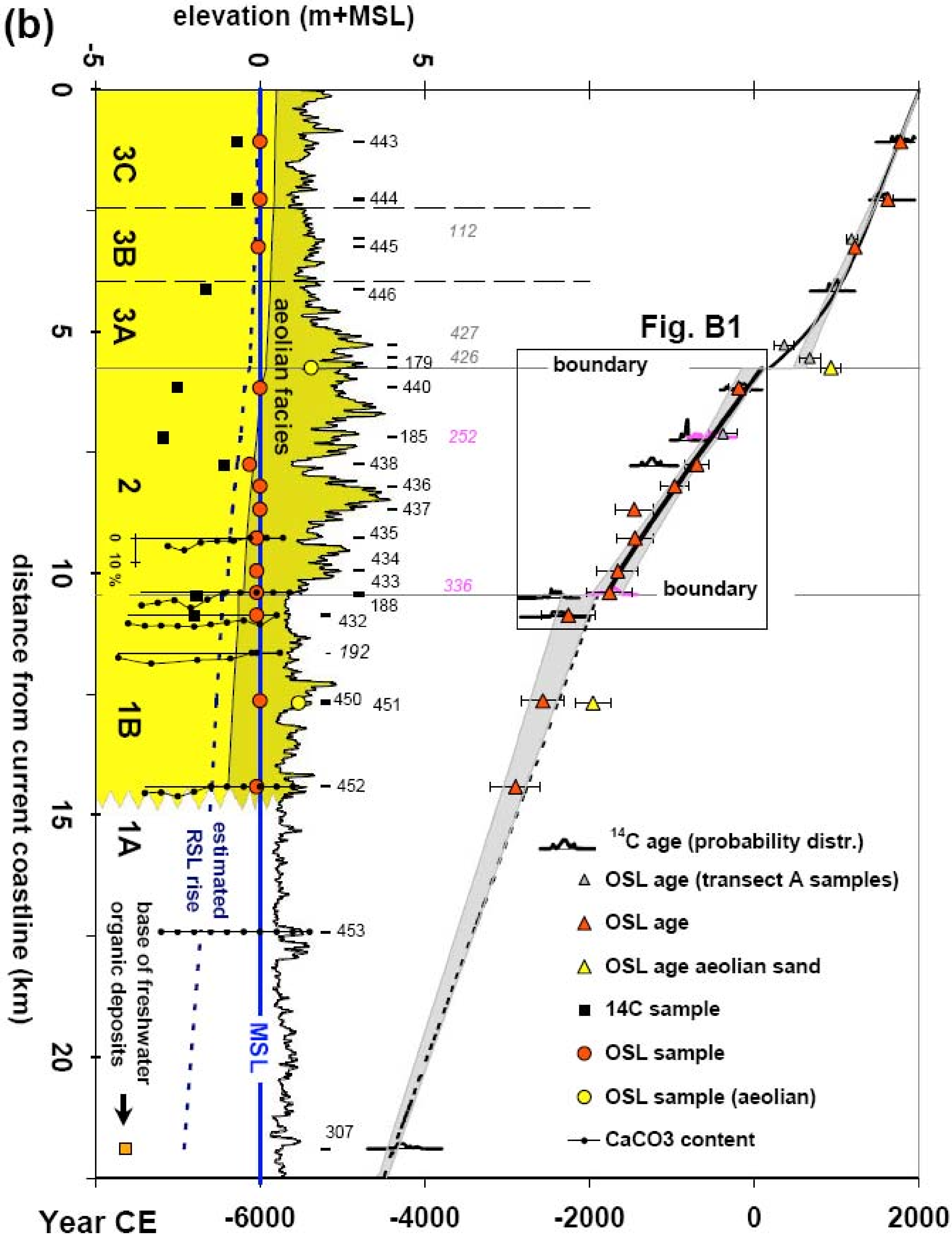
(b)
elevation (m+MSL)
distance from current coastline (km)
Year CE
aeolian facies
estimated RSL rise
base of freshwater organic deposits
MSL
Fig. B1
boundary
boundary
14C age (probability distr.)
OSL age (transect A samples)
OSL age
OSL age aeolian sand
14C sample
OSL sample
OSL sample (aeolian)
CaCO3 content

Figure 3b

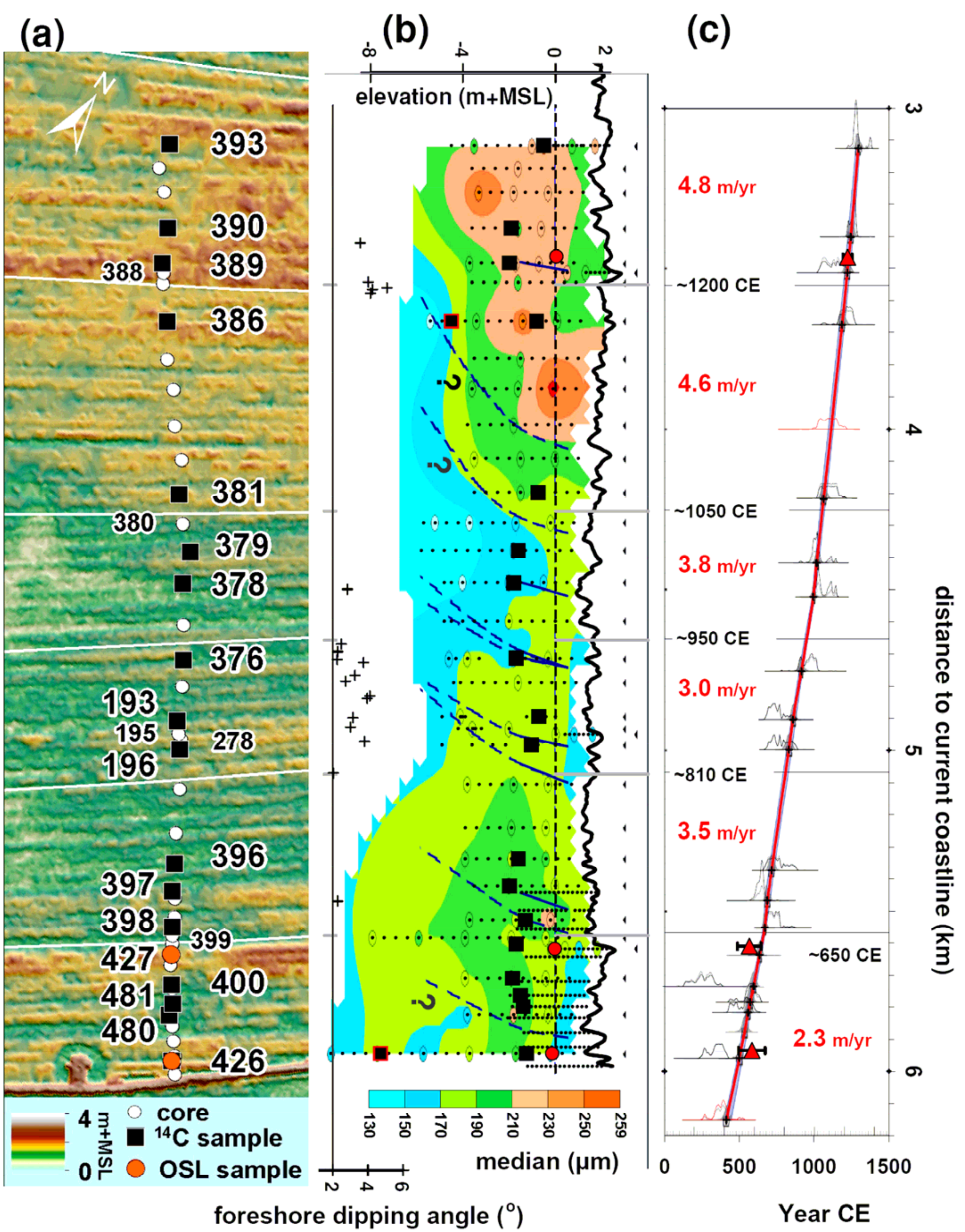

(a)
393
390
388
389
386
381
380
379
378
376
193
195
278
196
396
397
398
399
427
400
481
480
426
4
0
m+MSL
core
14C sample
OSL sample
(b)
elevation (m+MSL)
-8
-4
0
2
2
4
6
foreshore dipping angle (°)
130
150
170
190
210
230
250
259
median (µm)
(c)
4.8 m/yr
~1200 CE
4.6 m/yr
~1050 CE
3.8 m/yr
~950 CE
3.0 m/yr
~810 CE
3.5 m/yr
~650 CE
2.3 m/yr
0
500
1000
1500
Year CE
3
4
5
6
distance to current coastline (km)

Figure 4.

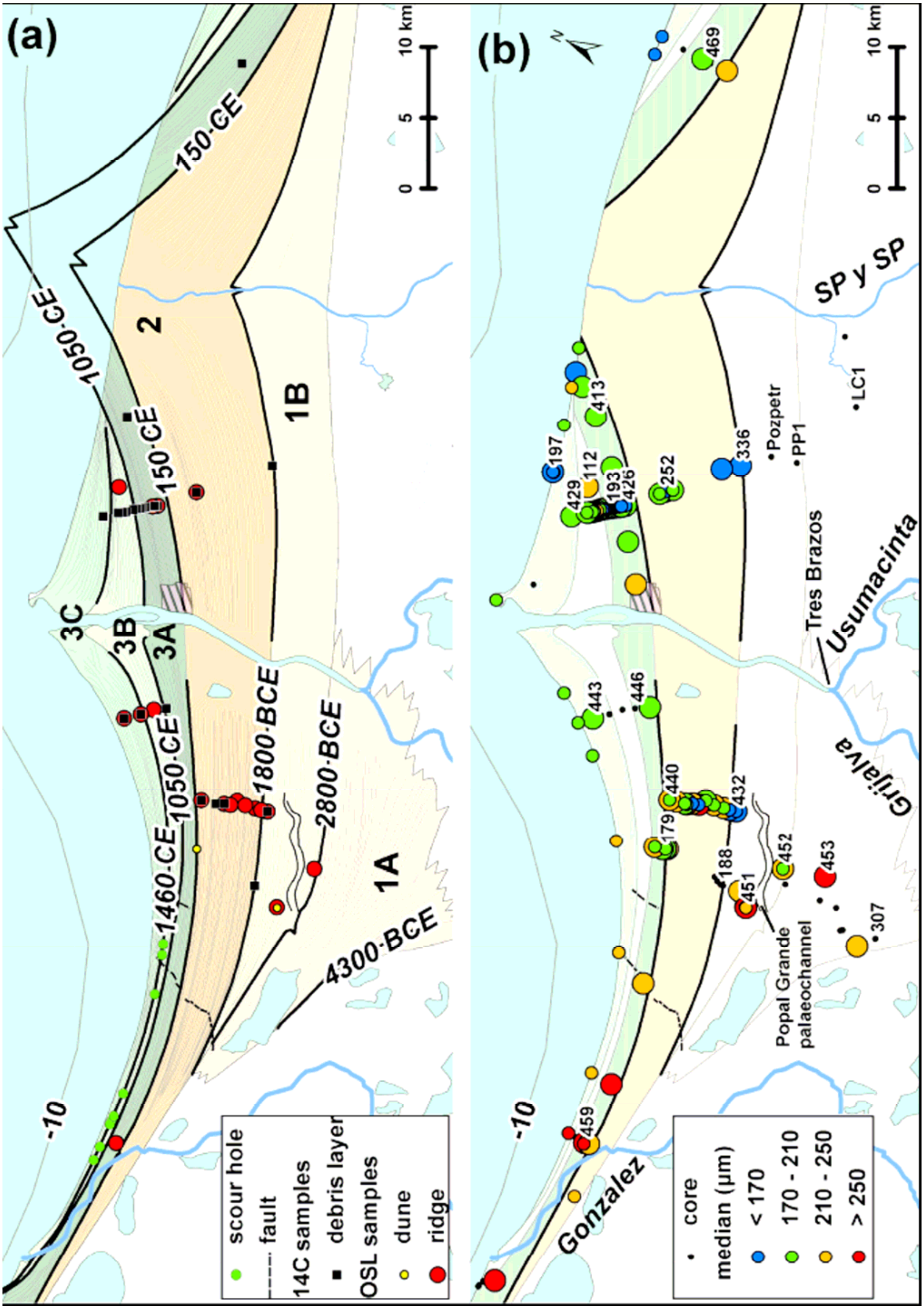
(a)
1050 CE
150 CE
2
1B
3C
3B
3A
1050 CE
1460 CE
1800 BCE
2800 BCE
1A
4300 BCE
-10
0 5 10 km
scour hole
fault
14C samples
debris layer
OSL samples
dune
ridge
(b)
N
SP y SP
LC1
Pozpetr
PP1
Tres Brazos
Usumacinta
Grijalva
Popal Grande palaeochannel
Gonzalez
-10
core
median (µm)
< 170
170 - 210
210 - 250
> 250
0 5 10 km

Figure 5

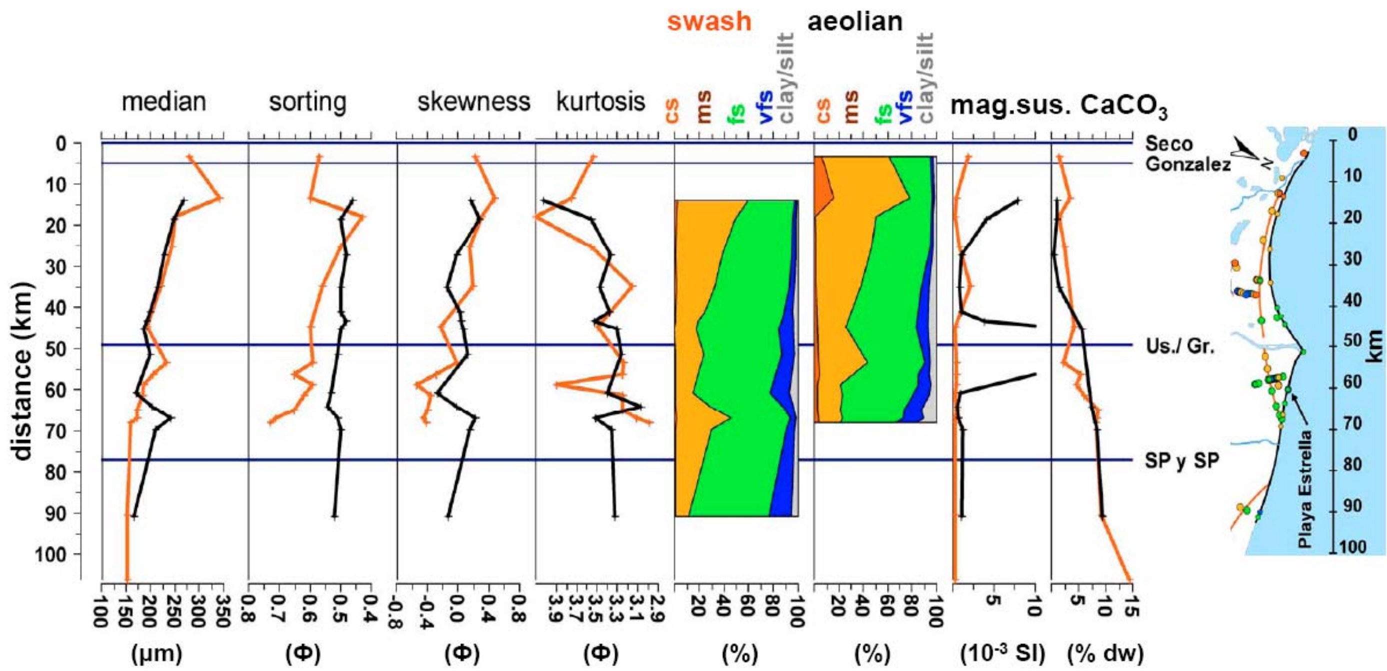

Figure 6.

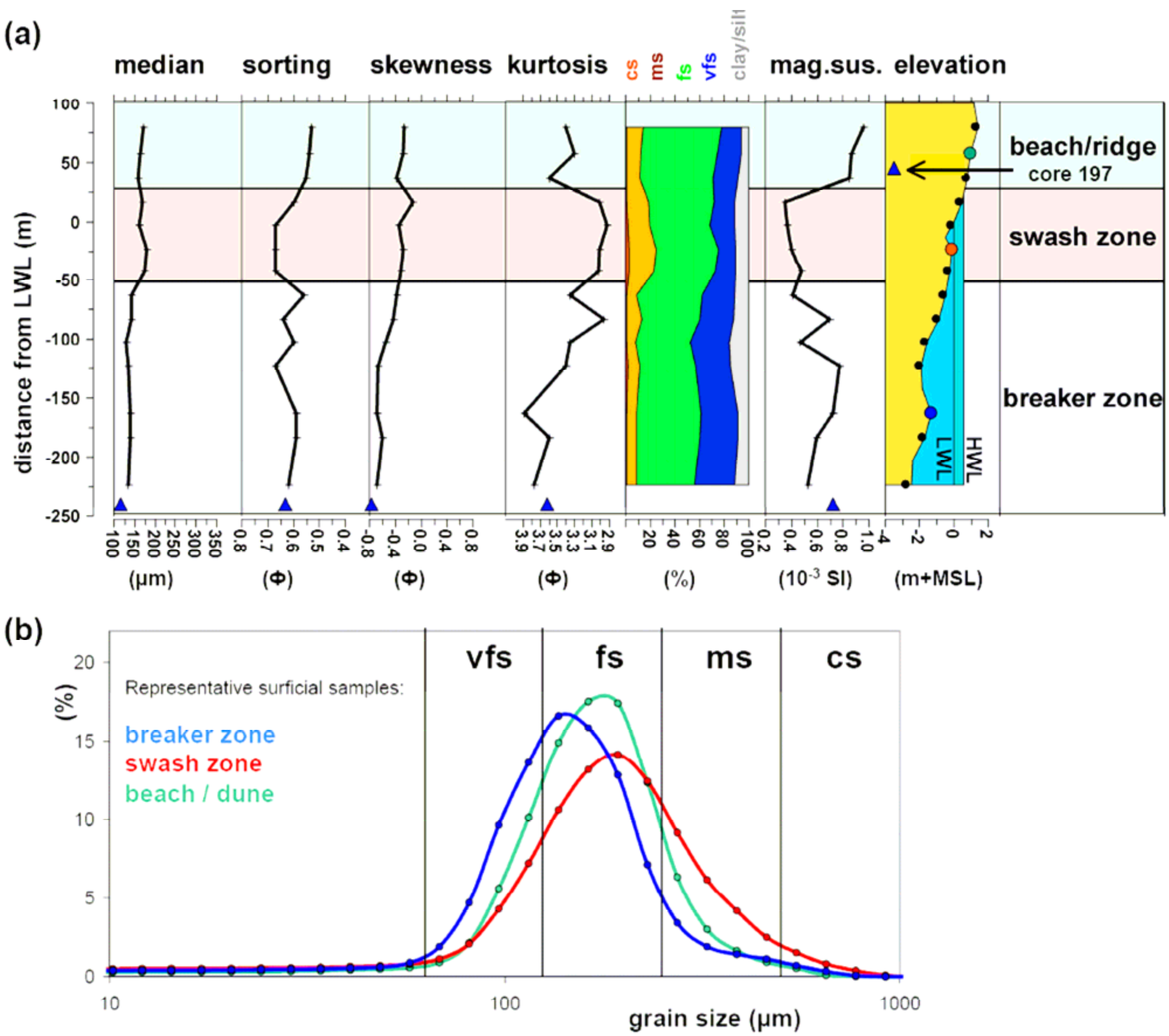

Figure 7

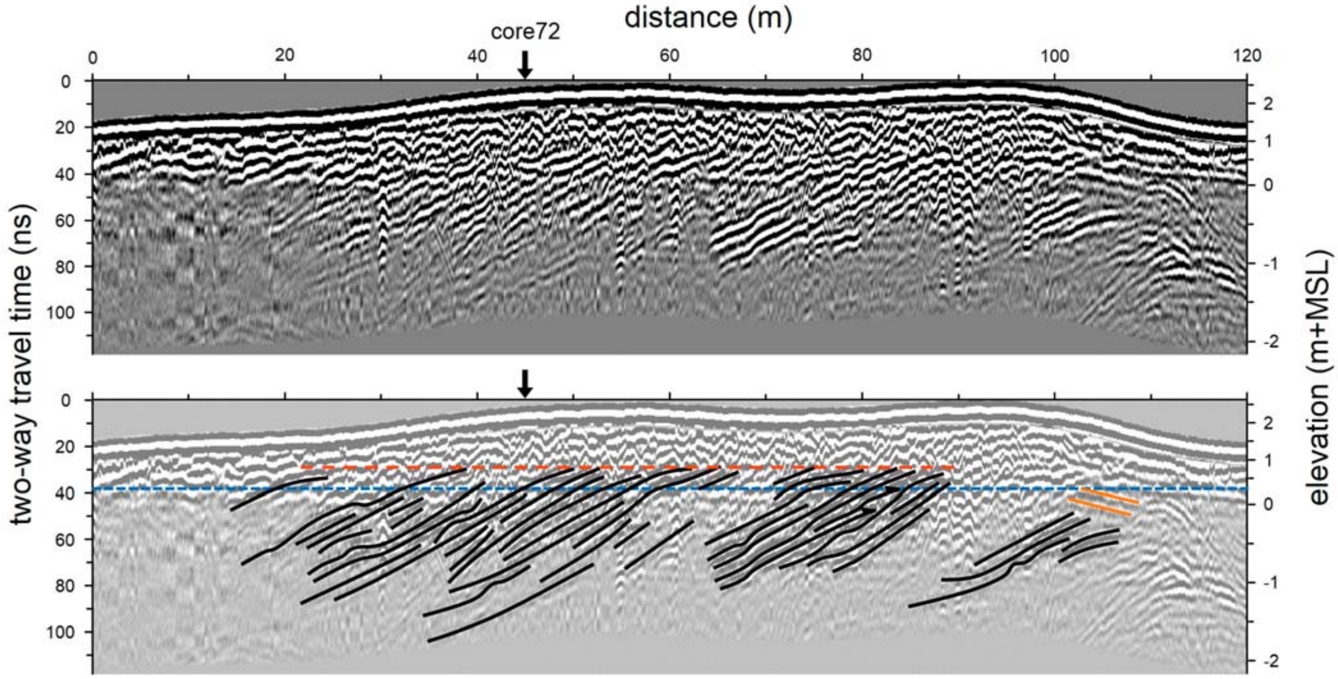

Figure 8

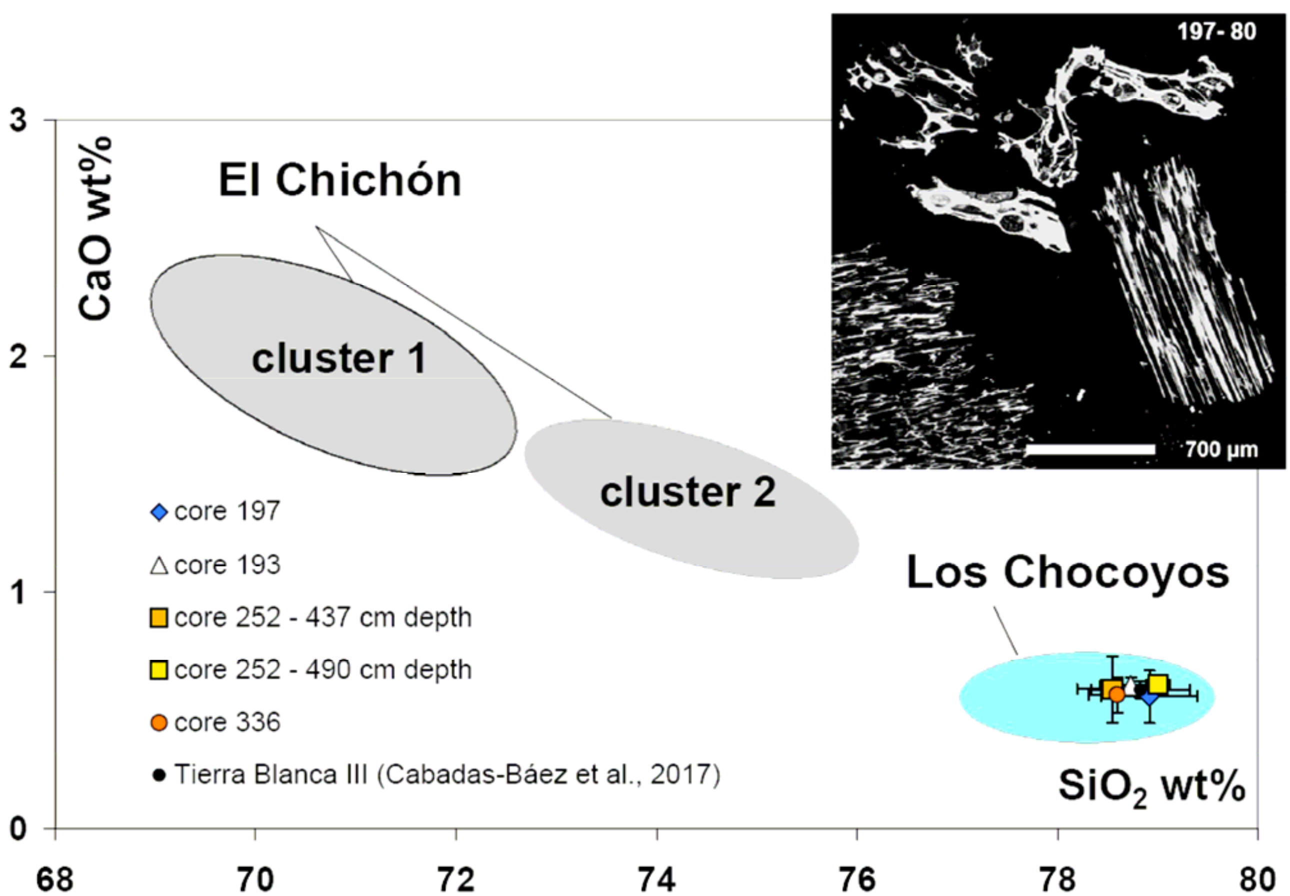

Figure 9.

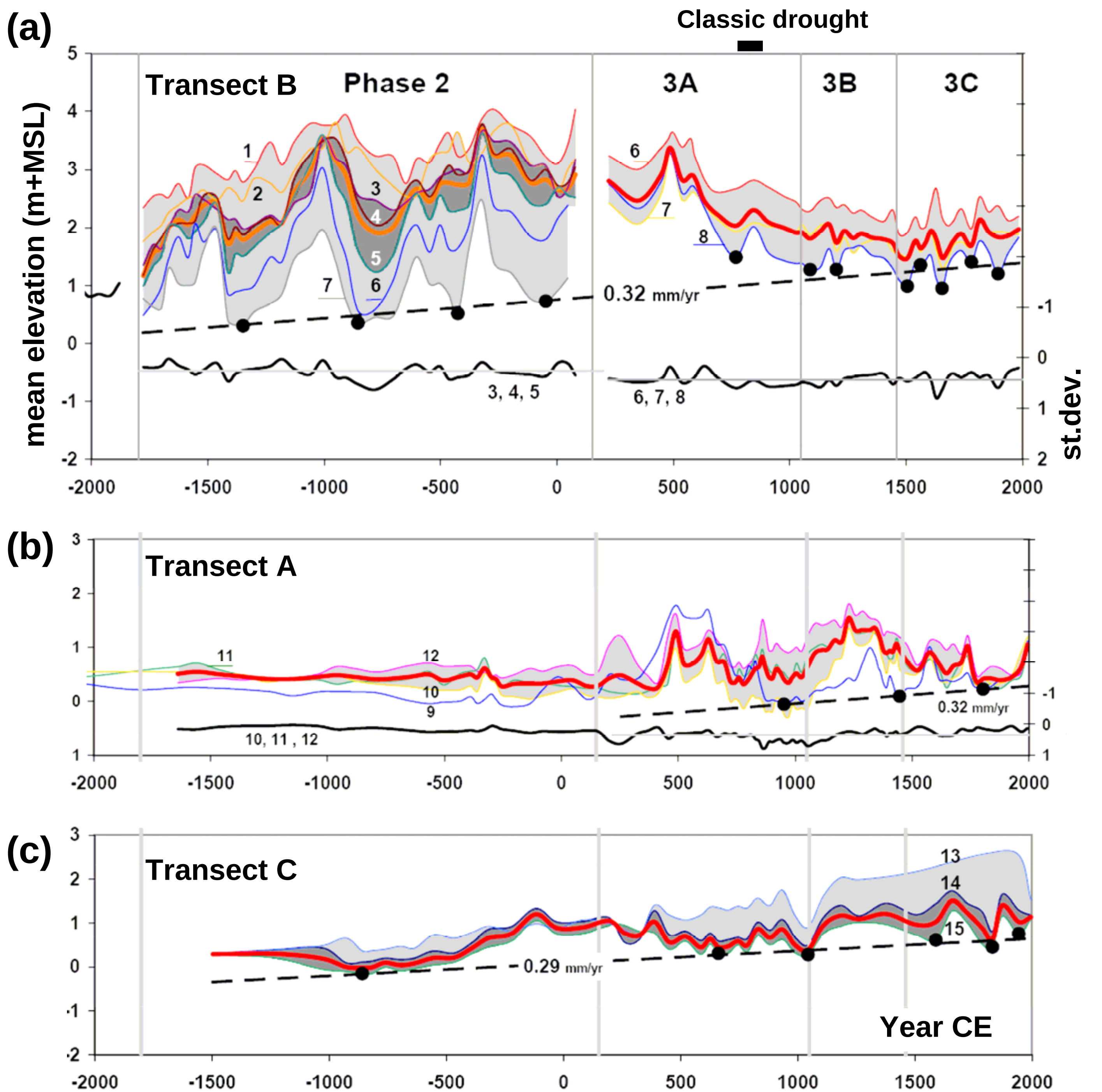

(a)
Classic drought
Transect B
Phase 2
3A
3B
3C
mean elevation (m+MSL)
st.dev.
0.32 mm/yr
3, 4, 5
6, 7, 8
(b)
Transect A
0.32 mm/yr
10, 11 , 12
(c)
Transect C
0.29 mm/yr
Year CE

Figure 10.

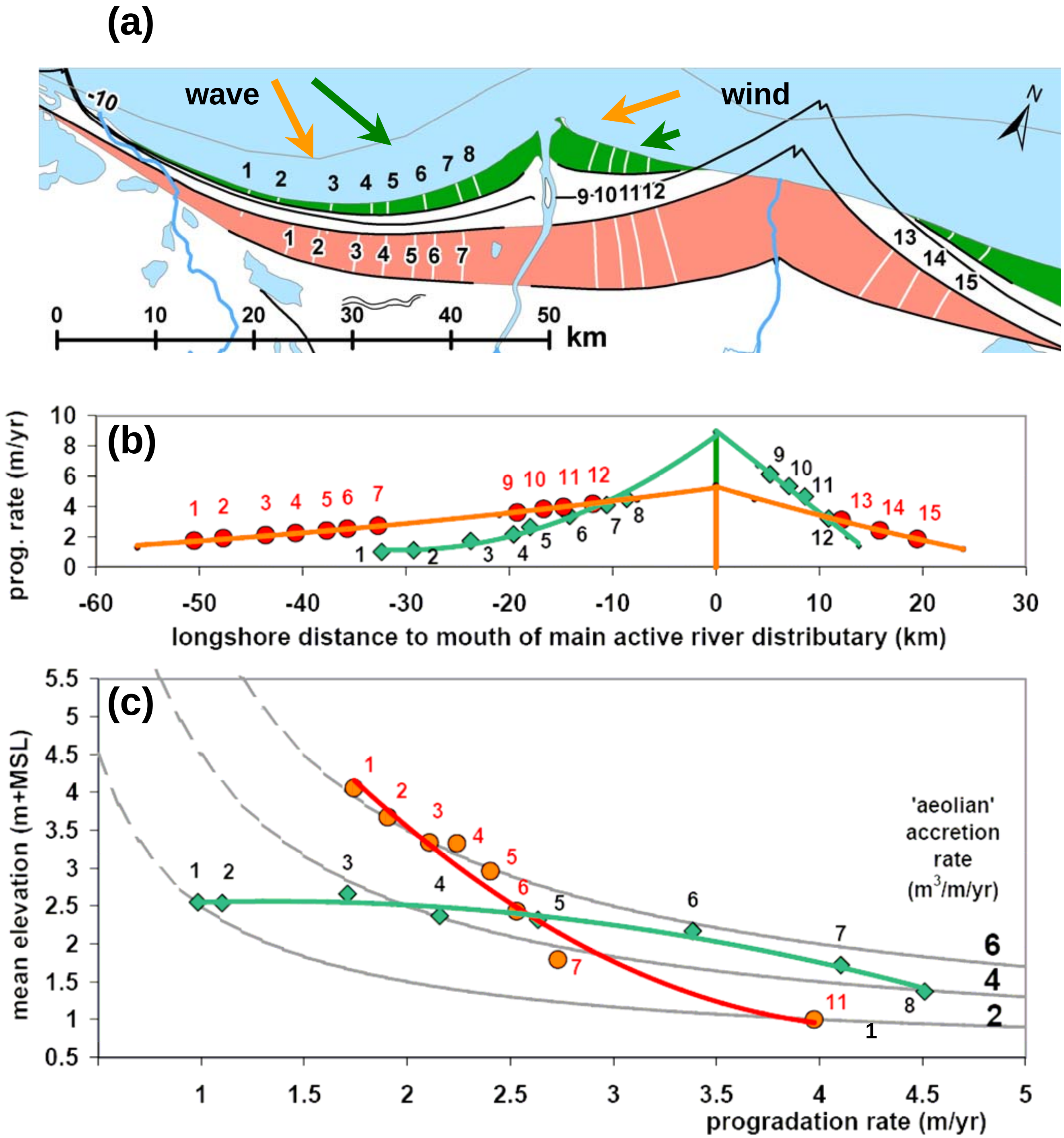
(a)
wave
wind
-10
N
1 2 3 4 5 6 7 8
9 10 11 12
1 2 3 4 5 6 7
13 14 15
0 10 20 30 40 50 km
(b)
prog. rate (m/yr)
longshore distance to mouth of main active river distributary (km)
(c)
mean elevation (m+MSL)
progradation rate (m/yr)
'aeolian' accretion rate (m3/m/yr)
6
4
2

Figure 11.

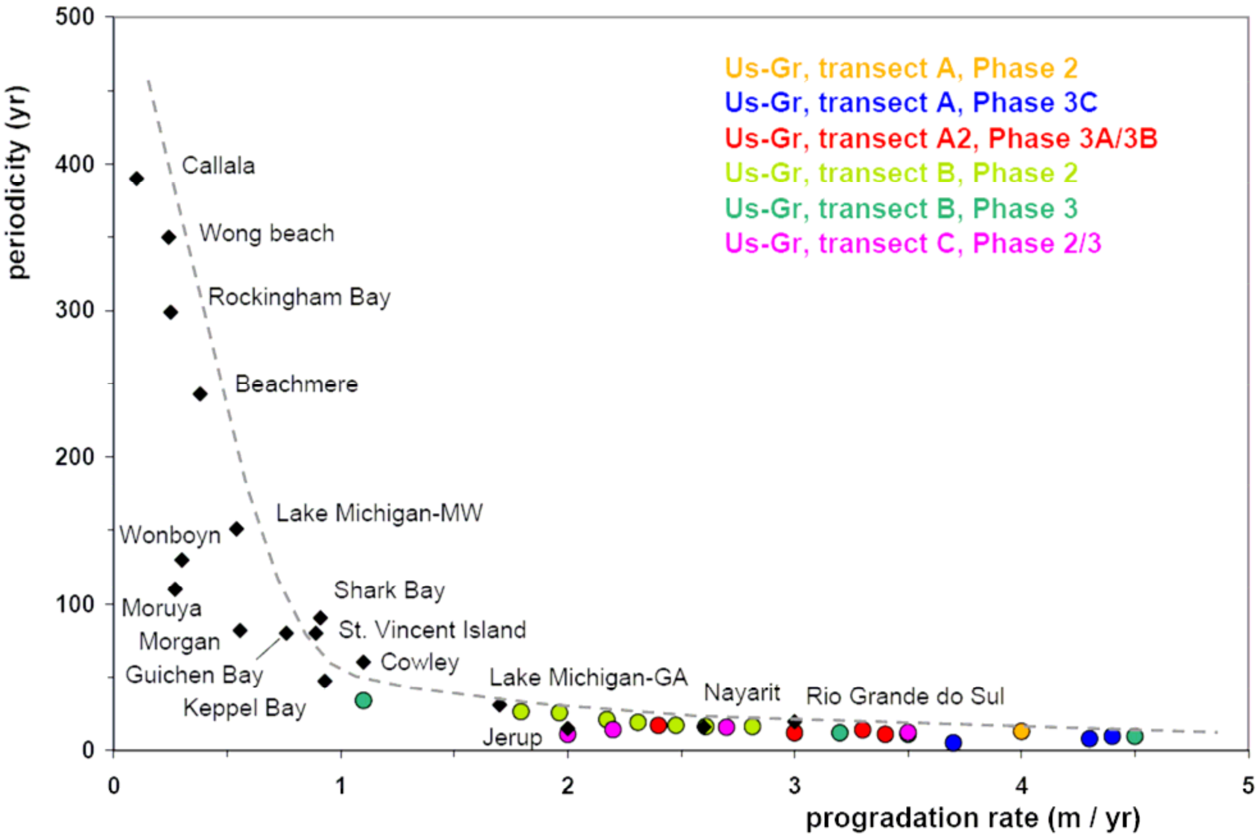

Figure 12

Table 1.

catchment	areal extent (km2)	(%)	average annual precipitation (mm/yr) [1]	average annual discharge (m^3/s) [2]	excess rainfall (%)
Usumacinta	70714	58	2150	2000	41
Grijalva	37471	31	1500	750	42
Sierra/Chilapa system	12840	11	2550	600	58

1. mean value for the watershed, calculated over the period 1950-2000 (WorldClim version 1.4 (release 3); Hijmans et al., 2005)
2. estimated valued based on measured discharges at the different hydrological stations (Banco Nacional de Datos dee Aguas Superficiales, consulted in June 2016)

Table 2.

phase	time range Year CE	transect	distance (km)	duration (yr)	mean elevation (m+MSL)	number of ridges	mean periodicity (yr)	mean progradation rate (m/yr)	total beach plain accretion ($m^3/m/yr$) [1]	mean aeolian accretion ($m^3/m/yr$)	(%)
3c	1460 - 2007	A	2.5	547	1.5 [2]	58	9.4	4.5	36 - 54	4.4 ± 2.1	11 ± 7
	1460 - 2007	B3	2.5	547	1.41	57	9.6	4.5	36 - 54	4.1 ± 2.1	10 ± 7
	1460 - 2007	C	1.1	547	1.37	50	10.9	2.0	16 - 24	1.7 ± 0.9	10 ± 7
3b	1050 - 1460	A	1.6	410	2.1 [2]	59	6.9	4.0	32 - 48	6.6 ± 1.9	18 ± 8
	1050 - 1460	B3	1.4	410	1.49	37	11.1	3.5	28 - 42	4.2 ± 1.9	14 ± 8
	1050 - 1460	C	0.9	410	1.31	29	14.1	2.2	17 - 26	3.4 ± 1.8	18 ± 12
3a	150 - 1050	A	2.4	900	1.55 [2]	61	14.8	2.7	21 - 32	3.5 ± 1.3	15 ± 8
	150 - 1050	B3	1.9	900	2.03	47	19.1	2.1	17 - 25	3.5 ± 1.0	19 ± 9
	150 - 1050	C	3.1	900	0.78	74	12.2	3.5	28 - 42	1.8 ± 1.6	6 ± 6
2	-1800 - 150	A	7.8	1950	0.44	150	13.0	4.0	32 - 48	2.5 ± 1.9	8 ± 6
	-1800 - 150	B2	4.7	1950	2.21	120	16.3	2.4	19 - 29	5.8 ± 1.2	26 ± 10
	-1400 - 150	C	4.3	1550	0.47	98	15.8	2.7	22 - 33	1.5 ± 1.0	6 ± 5
1	-4300 - -1900	B1	11.1	2400	0.82	154	15.6	4.6	-	-	-

1. assuming an average thickness for the beach ridge deposits of 8 - 12 m
2. 1 m was added to the LiDAR-elevation data from 2008

Appendix A

Table A1

	sample	dist. along transect (m)	GrA	Age BP	sigma	extracted fraction	d13C (‰)	C (%)
TRANSECT A								
	debris layers within beach ridge sands							
	429-250L	2110	58037	300	35	leaf fragments	-27.39	49.78
A2[1)]	393-300L	3120	58032	715	35	leaf fragments	-30.25	45.26
A2	390-330L	3375	59436	755	30	leaf fragments	-29.45	49.48
A2	389-330L	3485	58031	900	40	leaf fragments	-30.48	52.21
A2	386-240L	3665	59755	820	40	leaf fragments	-31.97	51.93
A2	386-610L	3665	59751	940	50	leaf fragments	-30.52	49.28
A2	381-225L	4195	59753	935	35	leaf fragments	-31.12	55.98
A2	379-280L	4375	58030	1015	35	leaf fragments	-28.29	48.16
A2	378-280L	4475	59435	990	30	leaf fragments	-28.95	52.84
A2	376-290L	4710	59752	1075	40	leaf fragments	-28.29	42.98
A2	193-171L	4890	55022	1250	30	leaf fragments	-30.05	61.50
A2	196-204L	4978	55023	1235	30	leaf fragments	-30.94	61.50
A2	396-270L	5330	59757	1255	40	leaf fragments	-30.94	51.96
A2	397-350L	5415	58033	1390	35	leaf fragments	-30.06	54.93
A2	398-260S	5520	59437	1270	30	squash seed	-29.45	49.48
A2	413-270L	5595	59438	1415	30	leaf fragments	-28.72	50.93
A2	400-295L	5700	59694	1775	40	leaf fragments	-30.31	45.30
A2	481-290L	5755	60873	1490	35	leaf fragments	-29.65	51.11
A2	480-290L	5790	60871	1525	35	leaf fragments	-29.74	51.38
A2	426-885L	5935	58035	1665	35	leaf fragments	-29.92	45.92
A2	426-255L	5935	58034	1690	40	leaf fragments	-29.75	52.56
	252-485L	8642	55021	2420	35	leaf fragments	-31.42	55.10
	252-485C	8642	55024	3290	30	charcoal	-24.66	73.70
	336-368L	14222	54940	3410	45	leaf fragments	-29.7	38.70
	336-368C	14222	55025	3990	35	charcoal	-25.02	68.20
	base of freshwater peat							
	Pozpetr.-78-82[2)]		UtC-11090	2055	59	charcoal/wood	-28.2	
	PP1-169-170[1)]		53751	3220	40	charred plant fragments	-21.55	53.40
	base of mangrove peat							
	LC1-315-320		55026	5030	35	charred plant fragments	-23.78	79.20
TRANSECT B								
	debris layers within beach ridge sands							
	443-230L	1075	58041	165	35	leaf fragments	-28.11	50.18
	444-150L	2270	58042	350	35	leaf fragments	-28.64	49.99
	446-275L	4134	58043	1060	40	leaf fragments	-29.53	52.03
	440-350L	6168	58040	2125	40	leaf fragments	-29.82	50.59
	185-471L	7195	55029	2665	35	leaf fragments	-28.61	42.30
	438-170L	7752	58039	3005	35	leaf fragments	-29.64	52.59
	188-310L	10468	55020	3930	35	leaf fragments	-30.33	51.60
	432-300L	10866	58144	3880	40	leaf fragments	-30.65	51.86
	base of freshwater peat							
	307-405-410S	21901	64320	5420	70	Asteraceae seeds	-28.08	
TRANSECT C								
	469-160L		58044	1210	35	leaf fragments	-29.63	49.70
	469-325L		58048	1360	35	leaf fragments	-29.51	46.92

1) Nooren et al., 2017
2) Nooren et al., 2009

Table A2

sample	NCL code	Lat.	Long.	comp. dist.[1]	depth	elev.	water content meas.	water content used		organic content		U^{238}		Th^{232}		K^{40}		unatten. doser. β		unatten. doser. γ		cosmic radiation		burial dose[2]		over-dispersion		dose rate		age		age		validity
		(°)	(°)	(m)	(m)	(m+MSL)	(% dw)	(% dw)	±	(% dw)	±	(Bq/kg)	±	(Bq/kg)	±	(Bq/kg)	±	(Gy/ka)	±	(Gy/ka)	±	(Gy/ka)	±	(Gy)	±	(%)	±	(Gy/ka)	±	(ka)	±	(Year CE)	±	
Transect A																																		
112	NCL-4112227	18.595	-92.594	3085	1.9	0	18.9	25	5	0.73	0.07	30.43	0.41	38.16	0.96	429	10	1.13	0.07	0.80	0.04	0.16	0.01	1.75	0.12	26	11	2.10	0.09	0.83	0.07	1182	70	Likely OK
427	NCL-1114072	18.570	-92.596	5280	2.3	0	27.7	25	5	1.26	0.13	13.67	0.17	14.71	0.37	724	15	1.39	0.09	0.65	0.03	0.15	0.01	3.6	0.2	30	4	2.20	0.1	1.65	0.12	363	120	Questionable
426	NCL-4213072	18.568	-92.595	5550	1.3	0	33.1	25	5	0.92	0.09	15.82	0.21	17.92	0.47	750	15	1.48	0.10	0.72	0.04	0.18	0.01	3.2	0.3	21	15	2.39	0.1	1.34	0.13	673	130	Likely OK
252	NCL-4112229	18.549	-92.575	7113	1.9	0	32.8	25	5	0.72	0.07	19.51	0.46	20.34	1.22	632	16	1.33	0.09	0.72	0.04	0.16	0.01	5.3	0.3	26	5	2.22	0.1	2.39	0.17	-378	170	Likely OK
Transect B																																		
443	NCL-4213078	18.530	-92.733	1075	1.6	0	25.9	25	5	0.87	0.09	20.50	0.32	23.05	0.76	577	13	1.25	0.08	0.71	0.04	0.16	0.01	0.5	0.04	20	8	2.13	0.09	0.24	0.02	1773	20	Likely OK
444	NCL-1114071	18.522	-92.726	2270	0.8	0	27.0	25	5	0.85	0.09	19.84	0.31	19.73	0.67	635	14	1.33	0.09	0.71	0.04	0.19	0.01	0.86[3]	0.12	69	18	2.24	0.1	0.39	0.06	1623	60	Likely OK
445	NCL-4213079	18.515	-92.719	3255	1.05	-0.05	29.0	25	5	0.84	0.08	14.83	0.27	15.26	0.68	725	15	1.41	0.09	0.67	0.04	0.18	0.01	1.79	0.08	7	6	2.28	0.1	0.79	0.05	1223	50	OK
179	NCL-4112228	18.452	-92.793	5750	0.55	1.55	4.7	5	3	1.78	0.18	18.87	0.30	23.12	1.58	612	13	1.60	0.09	0.86	0.05	0.20	0.01	2.9	0.3	33	9	2.66	0.1	1.08	0.12	932	120	Questionable
440	NCL-4213077	18.463	-92.761	6168	1	0	23.2	25	5	0.77	0.08	17.61	0.22	19.95	0.49	624	13	1.29	0.08	0.69	0.04	0.19	0.01	4.8	0.2	17	3	2.17	0.09	2.20	0.13	-187	130	OK
438	NCL-4213076	18.449	-92.757	7752	0.92	-0.32	26.2	25	5	0.52	0.05	16.13	0.28	19.16	0.67	627	13	1.30	0.08	0.69	0.04	0.19	0.01	5.9	0.2	10	4	2.18	0.09	2.71	0.15	-697	150	OK
436	NCL-1114073	18.445	-92.756	8199	2.2	0	24.8	25	5	0.87	0.09	15.72	0.23	18.32	0.53	643	13	1.30	0.08	0.68	0.04	0.15	0.01	6.4	0.2	12	3	2.14	0.09	2.98	0.17	-967	170	OK
437	NCL-4213075	18.442	-92.751	8678	1.5	0	29.9	25	5	1.00	0.10	18.22	0.30	21.42	0.74	661	14	1.36	0.09	0.72	0.04	0.17	0.01	7.8	0.4	18	6	2.26	0.1	3.47	0.23	-1457	230	OK
435	NCL-1114074	18.436	-92.751	9272	1.3	-0.1	25.2	25	5	0.93	0.09	18.03	0.28	20.24	0.66	679	14	1.36	0.09	0.69	0.04	0.18	0.01	7.8	0.4	16	5	2.25	0.1	3.46	0.23	-1447	230	OK
434	NCL-4213074	18.430	-92.751	9953	2.7	-0.1	25.8	25	5	1.05	0.11	14.56	0.25	16.65	0.68	658	14	1.31	0.09	0.66	0.04	0.14	0.01	7.8	0.4	23	4	2.13	0.09	3.67	0.25	-1657	250	Likely OK
433	NCL-1114075	18.426	-92.750	10398	1.5	-0.1	26.1	25	5	0.68	0.07	18.86	0.23	21.46	0.50	632	13	1.32	0.09	0.71	0.04	0.17	0.01	8.3	0.5	22	4	2.20	0.09	3.77	0.28	-1757	280	Likely OK
432	NCL-4213073	18.422	-92.749	10866	1.1	-0.1	25.1	25	5	0.25	0.03	14.78	0.26	16.49	0.66	594	13	1.21	0.08	0.63	0.03	0.18	0.01	8.7	0.5	23	4	2.03	0.09	4.27	0.33	-2257	330	Likely OK
450	NCL-4213080	18.390	-92.805	12637	1.05	0	20.9	25	5	0.58	0.06	13.06	0.24	15.49	0.61	529	12	1.08	0.07	0.56	0.03	0.18	0.01	8.4	0.3	12	3	1.83	0.08	4.58	0.26	-2567	260	OK
451	NCL-4213081	18.390	-92.806	12684	1.48	1.17	3.1	5	3	0.86	0.09	12.18	0.17	13.66	0.35	566	12	1.37	0.08	0.66	0.03	0.18	0.01	8.8	0.3	15	2	2.23	0.08	3.97	0.21	-1957	210	OK
452	NCL-1114076	18.379	-92.771	14412	1.6	-0.1	24.5	25	5	0.63	0.06	14.69	0.17	16.62	0.33	595	12	1.21	0.08	0.62	0.03	0.16	0.01	9.8	0.4	22	3	2.00	0.08	4.91	0.3	-2897	300	Likely OK
459	NCL-4213082	18.420	-92.994		0.7	-0.1	22.0	25	5	0.58	0.06	14.64	0.27	18.95	0.70	540	12	1.13	0.07	0.61	0.03	0.19	0.01	2.73	0.13	11	3	1.94	0.08	1.41	0.09	603	90	OK

1) composite distance from current coastline (m), projected along transect B (Fig. 3b)
2) the bootstrapped version of the Central Age Model (Cunningham and Wallinga, 2012) was applied to determine the burial dose of the samples.
3) for this sample the bootstrapped version of the Minimum Age Model (Cunningham and Wallinga, 2012) was applied to determine the burial dose. As over-dispersion input value (sigma_b) 18 ± 6% was used.
alpha dose rate of 0.010 ± 0.005 assumed for all samples

Table A3

core	depth (m)	n	SiO_2 (%)	±	TiO_2 (%)	±	Al_2O_3 (%)	±	FeO (%)	±	MnO (%)	±	MgO (%)	±	CaO (%)	±	Na_2O (%)	±	K_2O (%)	±	P_2O_5 (%)	±	S (%)	±	Cl (%)	±	total (%)	before norm.
197	0.8	10	78.87		0.10		12.28		0.56		0.08		0.09		0.57		3.02		4.27		0.01		0.01		0.12		100	97.34
				0.40		0.02		0.17		0.10		0.04		0.02		0.10		0.42		0.35		0.02		0.01		0.01		1.17
193[1]	5	7	78.72		0.10		12.36		0.55		0.06		0.09		0.60		3.19		4.19		0.01		0.01		0.11		100	98.09
				0.30		0.02		0.10		0.04		0.06		0.01		0.03		0.21		0.09		0.01		0.02		0.02		0.49
252	4.4	14	78.52		0.11		12.24		0.69		0.06		0.09		0.60		3.38		4.18		0.01		0.01		0.12		100	98.07
				0.38		0.03		0.17		0.24		0.04		0.05		0.17		0.12		0.48		0.02		0.02		0.01		0.49
252	4.9	10	79.00		0.10		12.19		0.52		0.06		0.09		0.61		3.10		4.20		0.01		0.02		0.11		100	97.51
				0.19		0.02		0.17		0.07		0.05		0.01		0.04		0.20		0.15		0.01		0.03		0.01		0.66
336	3.2	13	78.56		0.10		12.15		0.64		0.07		0.08		0.55		3.30		4.39		0.01		0.02		0.12		100	98.41
				0.31		0.01		0.13		0.19		0.03		0.01		0.08		0.14		0.22		0.02		0.02		0.03		0.39

		n	SiO_2 (%)	±	TiO_2 (%)	±	Al_2O_3 (%)	±	FeO (%)	±	MnO (%)	±	MgO (%)	±	CaO (%)	±	Na_2O (%)	±	K_2O (%)	±	BaO (%)	±	NiO (%)	±	Cr_2O_3 (%)	±		
TB III[2]		14	78.83		0.10		12.84		0.58		0.07		0.08		0.59		2.72		4.09		0.11		0.01		0.00		100	97.98
				0.49		0.01		0.37		0.05		0.02		0.01		0.04		0.39		0.22		0.04		0.02		0.00		2.57

1. pumice clast of 1.5 cm diameter
2. Tierra Blanca (Cabadas-Báez et al., 2017)

Appendix B

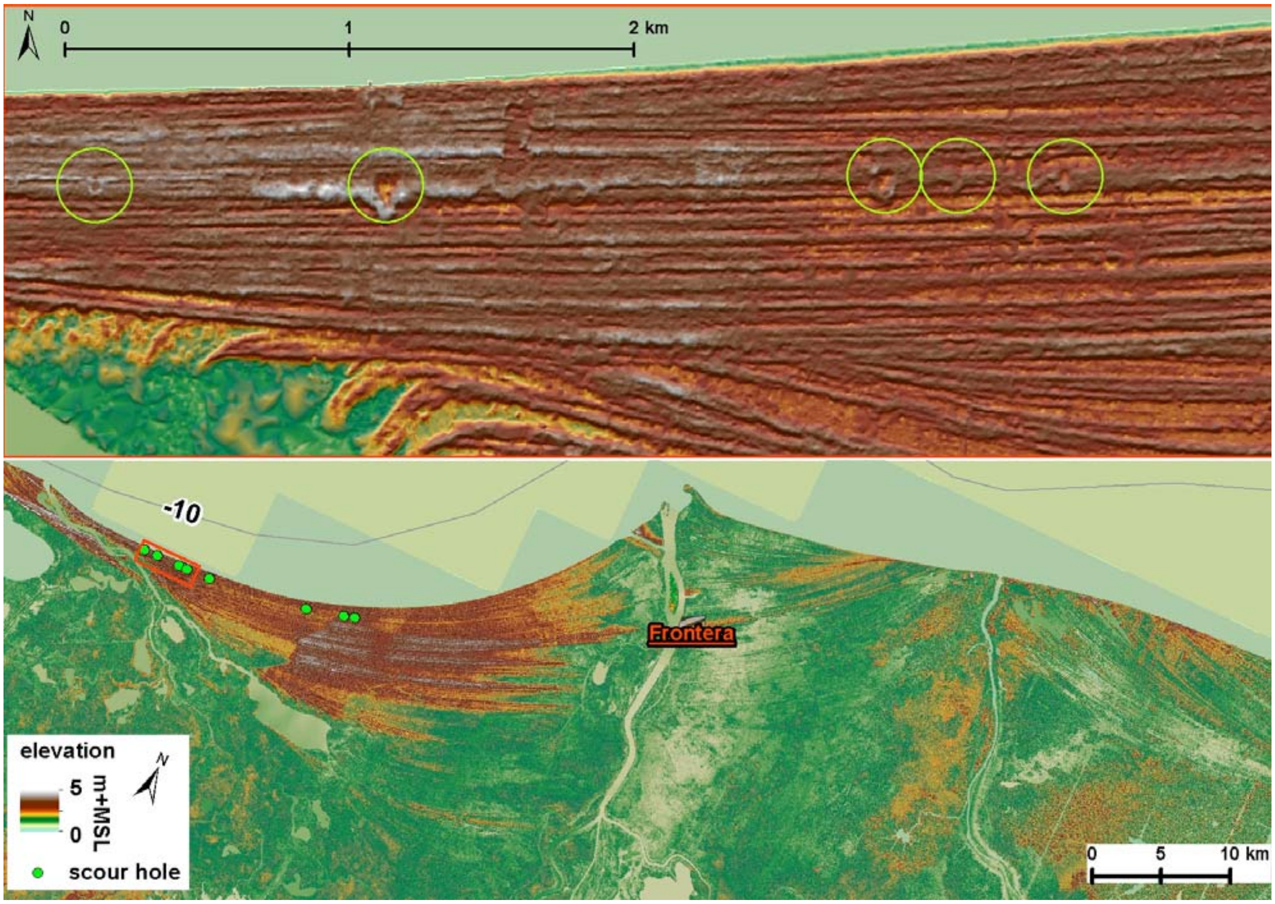

Figure B1

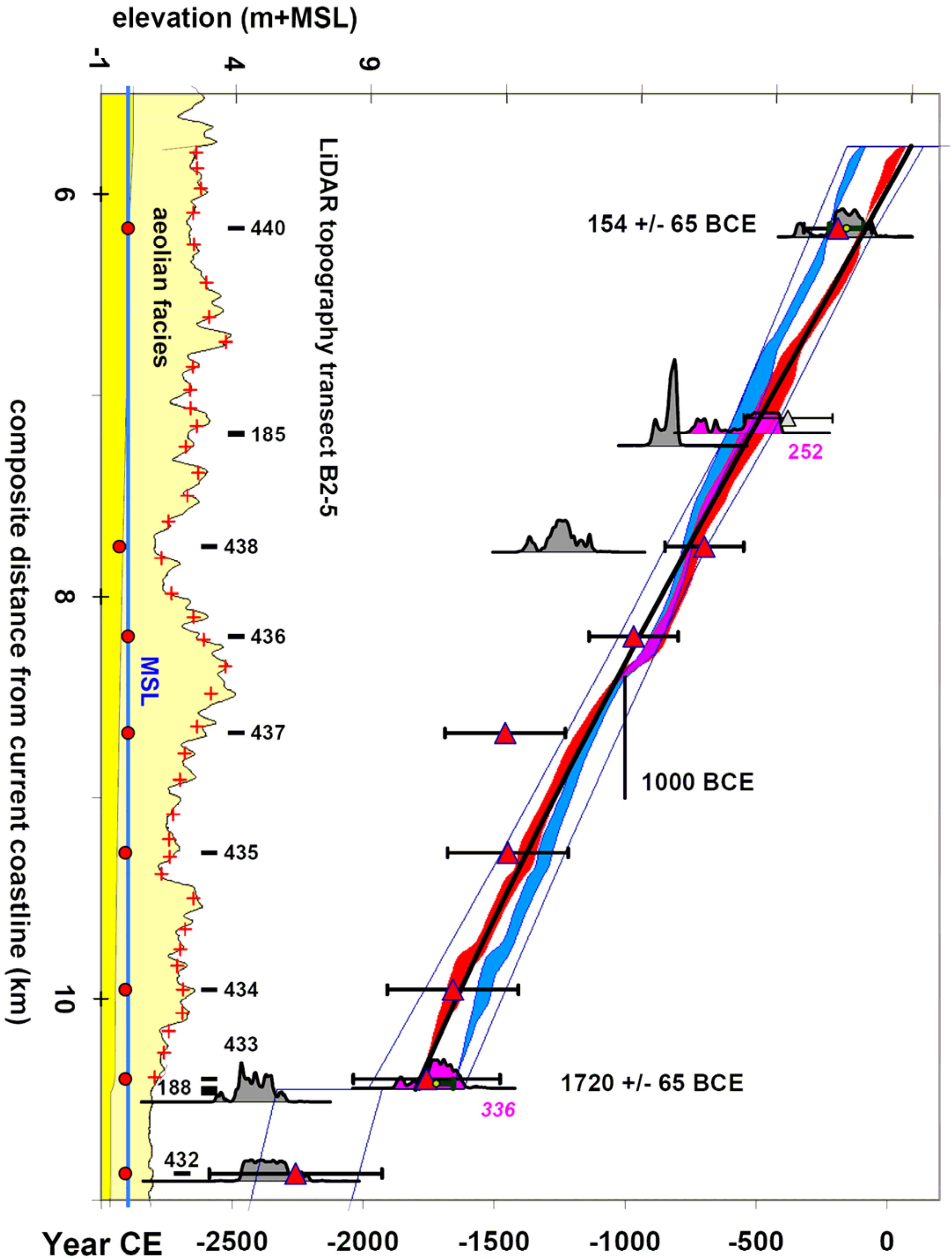
elevation (m+MSL)
-1
4
9
LiDAR topography transect B2-5
aeolian facies
MSL
440
185
438
436
437
435
434
433
188
432
154 +/- 65 BCE
252
1000 BCE
1720 +/- 65 BCE
336
composite distance from current coastline (km)
6
8
10
Year CE
-2500
-2000
-1500
-1000
-500
0

Figure B2

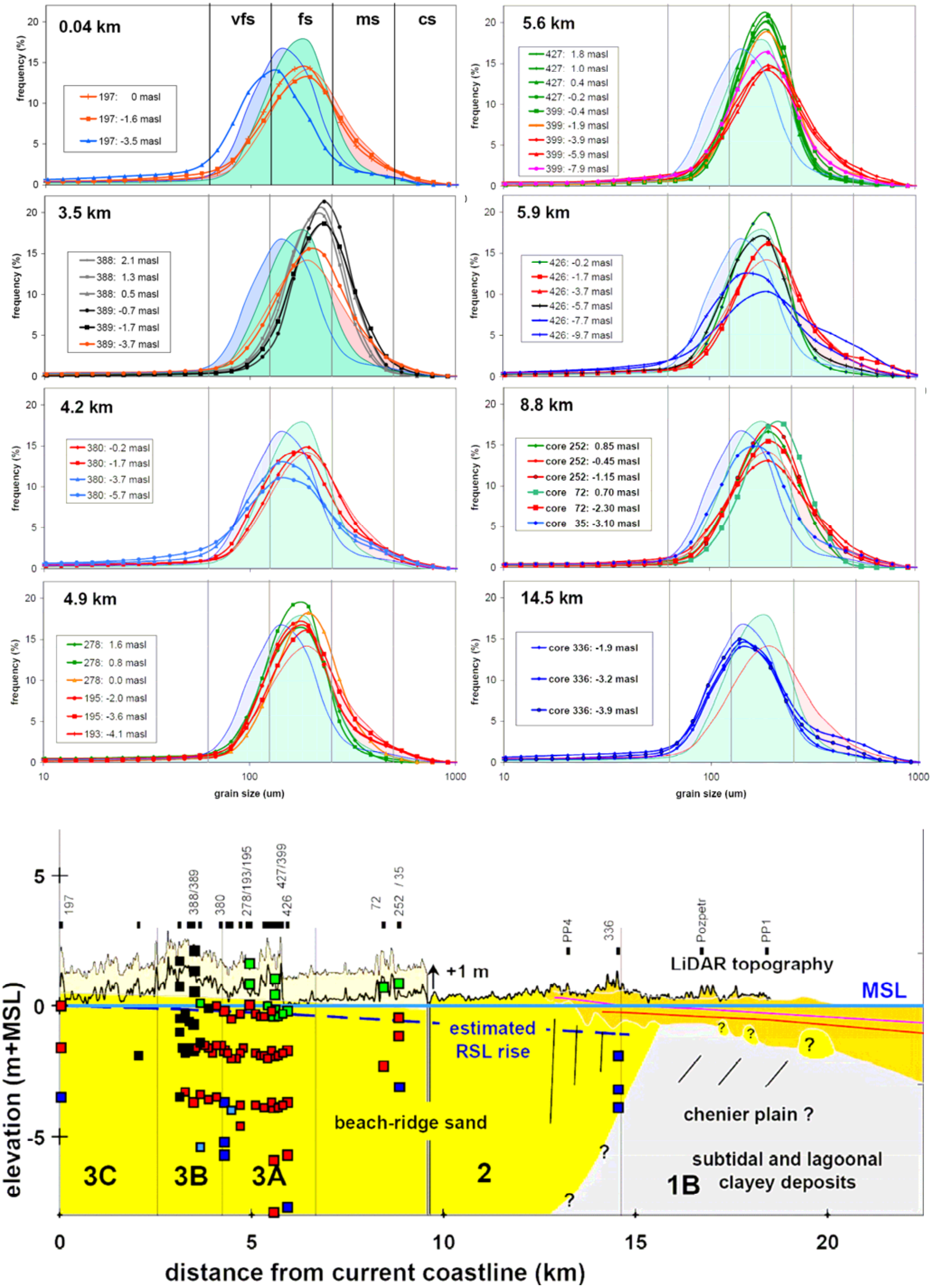
0.04 km
vfs
fs
ms
cs
197: 0 masl
197: -1.6 masl
197: -3.5 masl
5.6 km
427: 1.8 masl
427: 1.0 masl
427: 0.4 masl
427: -0.2 masl
399: -0.4 masl
399: -1.9 masl
399: -3.9 masl
399: -5.9 masl
399: -7.9 masl
3.5 km
388: 2.1 masl
388: 1.3 masl
388: 0.5 masl
389: -0.7 masl
389: -1.7 masl
389: -3.7 masl
5.9 km
426: -0.2 masl
426: -1.7 masl
426: -3.7 masl
426: -5.7 masl
426: -7.7 masl
426: -9.7 masl
4.2 km
380: -0.2 masl
380: -1.7 masl
380: -3.7 masl
380: -5.7 masl
8.8 km
core 252: 0.85 masl
core 252: -0.45 masl
core 252: -1.15 masl
core 72: 0.70 masl
core 72: -2.30 masl
core 35: -3.10 masl
4.9 km
278: 1.6 masl
278: 0.8 masl
278: 0.0 masl
195: -2.0 masl
195: -3.6 masl
193: -4.1 masl
14.5 km
core 336: -1.9 masl
core 336: -3.2 masl
core 336: -3.9 masl
frequency (%)
grain size (um)
elevation (m+MSL)
distance from current coastline (km)
197
388/389
380
278/193/195
427/399
426
72
252 / 35
PP4
336
Pozpetr
PP1
LiDAR topography
+1 m
MSL
estimated
RSL rise
beach-ridge sand
chenier plain ?
subtidal and lagoonal
clayey deposits
3C
3B
3A
2
1B

Figure B3

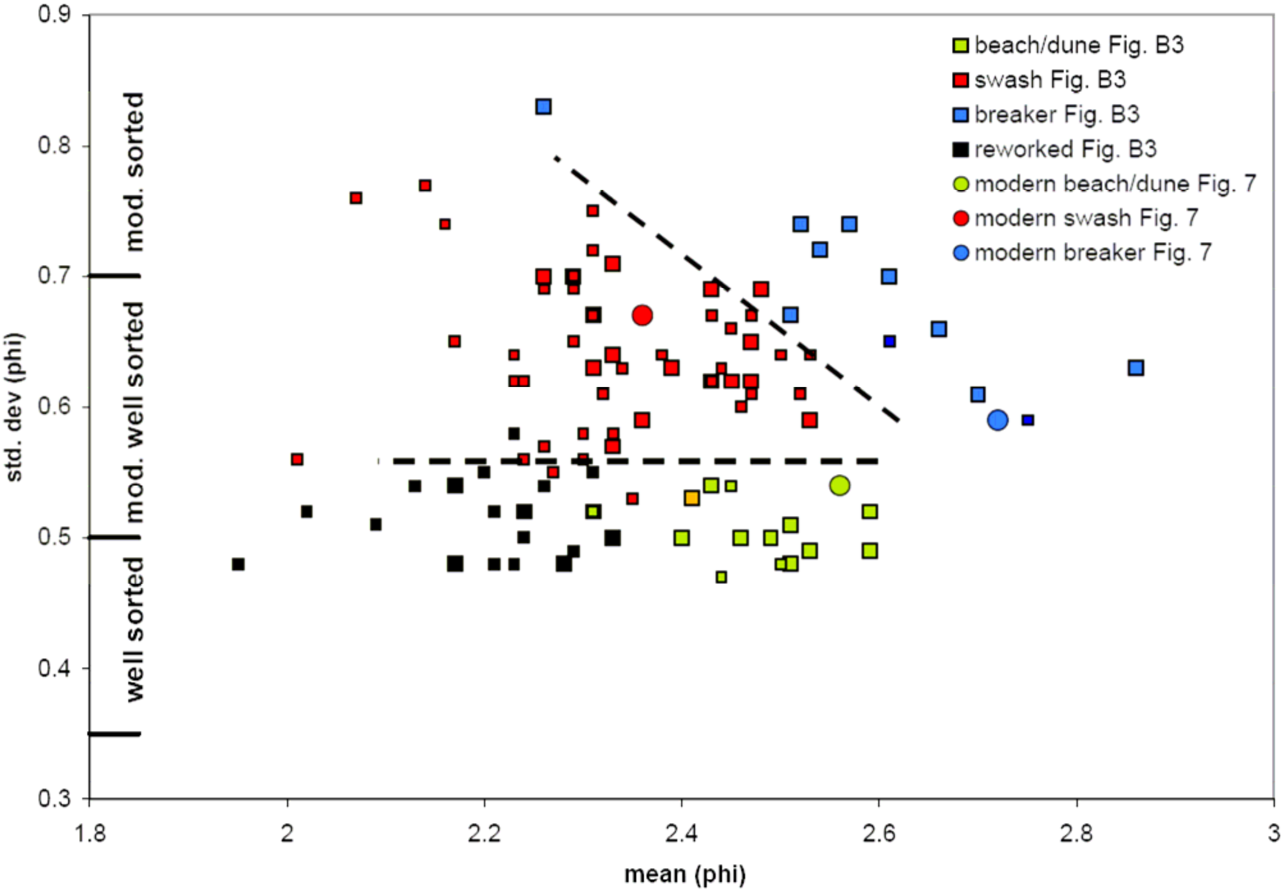
beach/dune Fig. B3
swash Fig. B3
breaker Fig. B3
reworked Fig. B3
modern beach/dune Fig. 7
modern swash Fig. 7
modern breaker Fig. 7
mod. sorted
mod. well sorted
well sorted
std. dev (phi)
mean (phi)
0.9
0.8
0.7
0.6
0.5
0.4
0.3
1.8
2
2.2
2.4
2.6
2.8
3

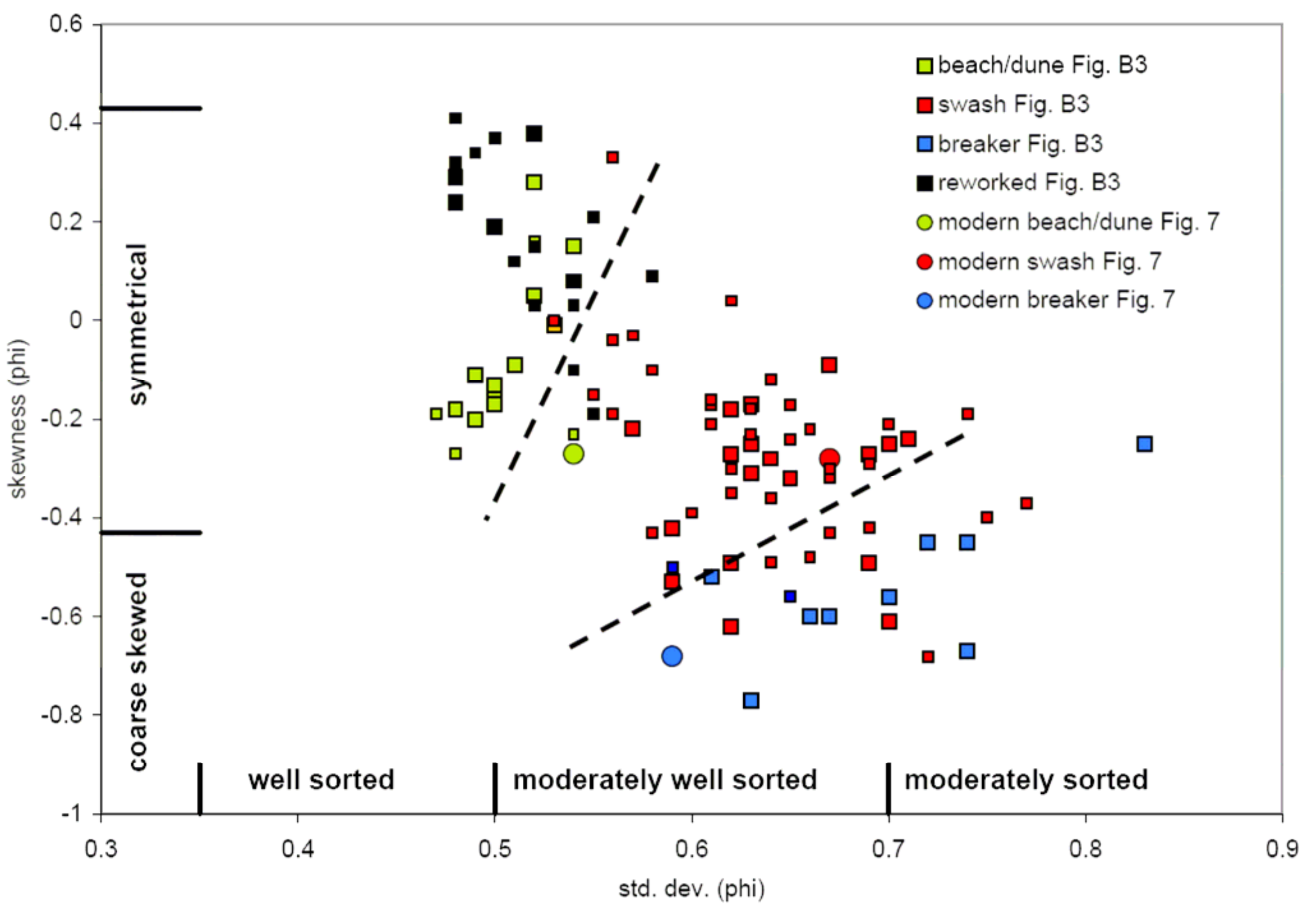
beach/dune Fig. B3
swash Fig. B3
breaker Fig. B3
reworked Fig. B3
modern beach/dune Fig. 7
modern swash Fig. 7
modern breaker Fig. 7
symmetrical
coarse skewed
skewness (phi)
well sorted
moderately well sorted
moderately sorted
std. dev. (phi)
0.6
0.4
0.2
0
-0.2
-0.4
-0.6
-0.8
-1
0.3
0.4
0.5
0.6
0.7
0.8
0.9

Figure B4